*J. Fluid Mech.* (1992), *vol.* 235, *pp.* 143–178
*Printed in Great Britain*

# Particle dispersion in the developing free shear layer. Part 1. Unforced flow

By B. J. LÁZARO AND J. C. LASHERAS
Department of Applied Mechanics and Engineering Sciences, University of California, San Diego, La Jolla, CA 92093-0411, USA

(Received 27 April 1990 and in revised form 9 March 1991)

An experimental investigation of the dispersion of small particles in a developing, high-Reynolds-number, turbulent, plane mixing layer is presented. Flow visualizations, laser attenuation and diffraction techniques as well as hot-wire anemometry are used to describe the evolution of the mean and instantaneous particle and gas flow fields. It is shown that the large scale turbulent motion existing in the mixing layer plays a central role in the dispersion of the particles. The mean particle concentration field is shown to be the result of a statistical distribution of streaks produced by the large-scale coherent component of the turbulent motion in the mixing layer. Furthermore, for every particle size, the spreading of the particle concentration thickness is found to occur at a smaller rate than the one characterizing the momentum of the turbulent carrier gas. Large particles are shown to initially disperse into the mixing layer less effectively than the small ones. However, when both downstream and cross-stream coordinates are non-dimensionalized with a characteristic length proportional to the square of the droplet diameter, a universal, particle-size independent dispersion field is found to exist.

## 1. Introduction

Understanding the particle–turbulence interaction problem is of great importance in a variety of practical applications. On many occasions, such as in liquid-spray-based combustors or chemical reactors, the effect that a turbulent motion has on the spatial, instantaneous distribution of the particles is the fundamental step controlling the performance of the process.

The common denominator in all these systems is the complexity that they possess both from an analytical and experimental point of view. The theoretical analysis presents difficulties associated with defining the transfer laws for mass, momentum and energy between the two phases, and the modification that the turbulent environment can have on these laws. From purely kinematic grounds, it is possible to obtain some results about the asymptotic behaviour of the parameters characterizing the dispersion of particles in a turbulent medium (Taylor 1921). The dynamical analysis, however, involves approximations that are, physically, hardly justifiable (Hinze 1975). In the general case in which the turbulence is anisotropic and inhomogeneous the transfer terms depend on the particle time history and the analysis becomes highly complex (Hunt 1985; Thompson 1987). Since the practical applications often include interactions between the particles and some free shear layer, it is precisely in these situations where the study of particle dispersion becomes more relevant. The identification of a quasi-orderly large-scale structure in this type of flow (Brown & Roshko 1974) has prompted a revision of the mechanisms thought to control the transport of particulates by anisotropic turbulence. In a recent review article, Crowe, Chung & Troutt (1988) have stressed the importance of the large-scale coherent component of the turbulent motion in the particle dispersion process, suggesting the possibility of encountering a range of particle sizes for which their dispersion would be maximized. Furthermore, recent numerical work in axisymmetric jets by Chung & Troutt (1988) and in mixing layers (Chein & Chung 1988) as well as preliminary experimental studies (Kobayashi *et al.* 1988; Lázaro & Lasheras 1989; Longmeir & Eaton 1989) indicate that the dispersion of small, heavy particles in free shear flows can exhibit rates surpassing those characterizing a passive scalar.

Experimental difficulties have hampered the characterization and physical understanding of this type of flow. Pioneer studies relied on individual analysis of photographic data (Snyder & Lumley 1971). In the past decade, however, there has been substantial development of experimental methods applied to particle flows. Particle sizing techniques based on small-angle laser diffraction scattering (Swithenbank *et al.* 1976) and laser-Doppler interferometry (Bachalo & Houser 1984) offer the possibility of extensive, fast and non-intrusive flow characterizations. Using laser scattering techniques, it is also possible to perform automated measurements of particle Lagrangian statistics (Call & Kennedy 1990).

Using a variety of non-intrusive optical techniques, the present investigation concentrates on the momentum exchange processes between the particles and the surrounding turbulent fluid. For this purpose we will study an isothermal, inhomogeneous anisotropic turbulent plane mixing layer formed between a particle-laden and a particle-free gaseous stream. The physical justification of this choice is the central role played by the momentum transfer in the dispersion and mixing of discrete particles. Moreover, our study is limited to the case where the presence of the particles does not substantially alter the turbulent structure of the base fluid. Thus, we have restricted ourselves to the case in which the particle concentration is small.

In this paper we will study the evolution of the two-phase plane mixing layer under natural (unperturbed) conditions. In Part 2 (Lázaro & Lasheras 1992) the analysis of the evolution of the dispersion layer subjected to a periodic acoustic forcing will be presented.

## 2. Experimental facility

A schematic view of the flow generation apparatus is shown in figure 1. It consists of an atmospheric-pressure two-dimensional open-return wind tunnel placed horizontally. The plane mixing layer is created when a uniform-density spray of water droplets discharges into a stagnant air region. The carrier gas flow is created by a centrifugal compressor with a rectangular outlet cross-section of 53 × 16 cm. Located at the wind tunnel entrance is a flow conditioning section consisting of an 8 mm cell hexagonal honeycomb (50 mm long) and a 37 mesh screen. The particles are injected into the flow downstream of the conditioning section by means of a low-flow-disturbing particle generator composed of an array of 184 miniature air-blast atomization units. Each atomizer (figure 2) consists of $22G$ blunt needles. One of them is fed with compressed air and produces an air jet that is projected perpendicular to a distilled water capillary jet emanating from the other needle. The atomizer is supported by a stem consisting of two 1.6 mm copper tubes welded together. In this fashion, the atomizer has only a 1.6 mm cross-stream width. The design is similar to the one used in our previous investigation (Lázaro & Lasheras

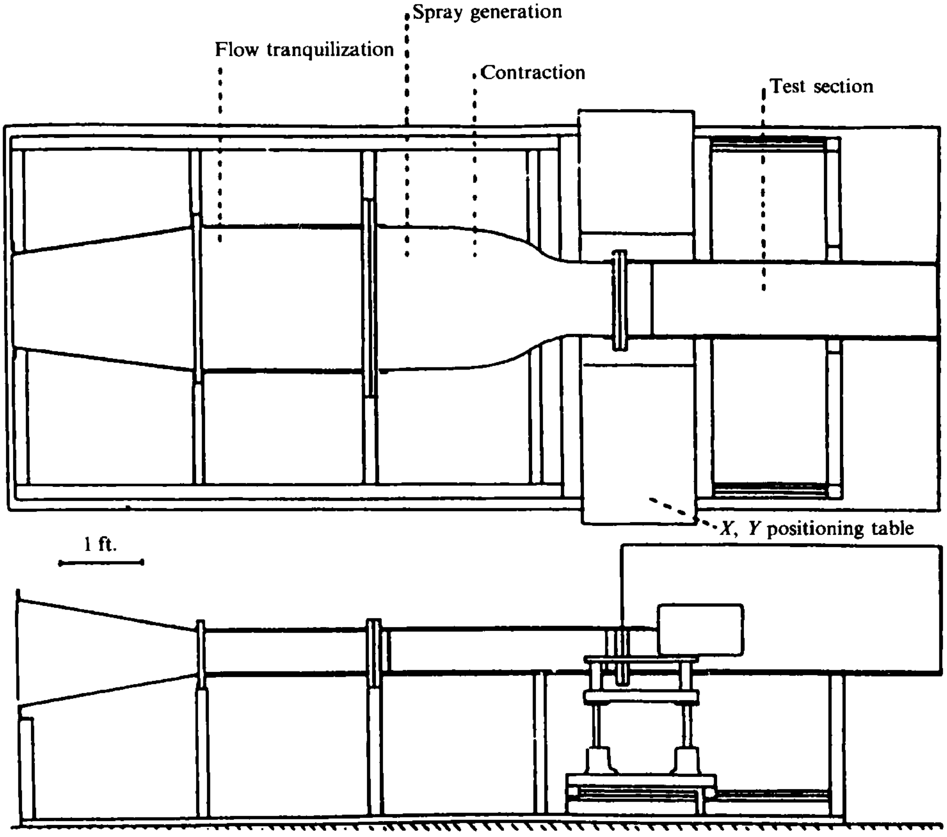

FIGURE 1. Flow generation apparatus.

FIGURE 2. Detail of an atomizer unit.

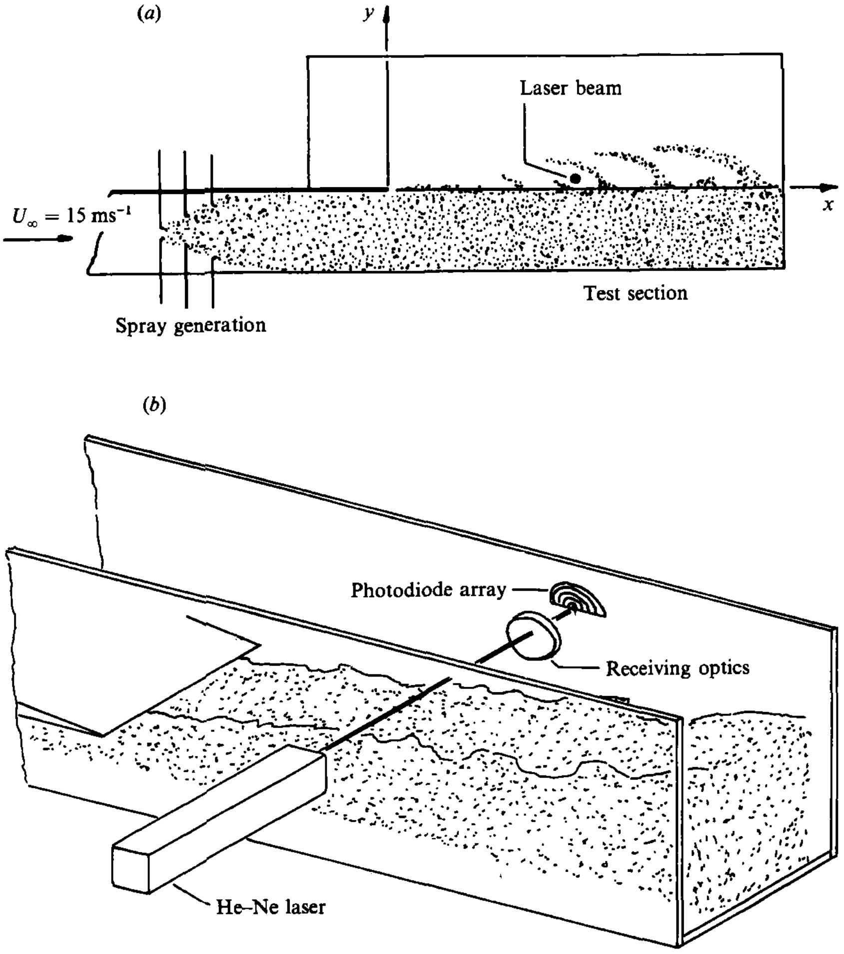

FIGURE 3. Test section and experimental set-up. (*a*) Coordinate system. (*b*) Perspective schematic view of the laser scattering arrangement.

1989) and has been proven to work efficiently in generating those particle sizes and concentrations typically encountered in practical applications without introducing appreciable disturbances in the flow. The atomizers are placed in the cross-stream plane and form an equidistant triangular mesh composed of eight horizontal rows. Each row contains 23 equally spaced units (15 mm horizontal separation distance). The water flow rate feeding each row is independently adjusted, thereby providing control of the free-stream particle concentration profile. To prevent wetting of the sidewalls at the test section, the four atomizer units closest to the walls in every row are operated with the atomization air jet only and no water supply. With this design the carrier gas flow has uniform properties throughout the spanwise coordinate. To homogenize the spray and to reduce the flow disturbance introduced by the atomizers, the air flow loaded with the spray droplets passes through a 50 cm long 2:1 contraction nozzle before discharging into the test section. The two-dimensional plane mixing layer is then formed at the end of a 1.5 mm thick aluminium splitter plate, when the particle-laden air stream discharges into a stagnant air region. Additional details on the design of the facility can be found in Lázaro (1989).

The total length of the test section is 114 cm, with the measurement window spanning the first 25 cm. The coordinate system used in this study (figure 3*a*) has its origin at the end of the splitter plate, with the $x$- and $y$-axes corresponding to the downstream and cross-stream coordinates respectively while $z$ is aligned with the homogeneous direction of the plane shear layer.

Owing to the extensive use of optical, non-intrusive flow diagnostics, special attention was given to controlling the wind tunnel's mechanical vibration. The blower and the tunnel are separated by means of a flexible joint and the electric motor driving the compressor is mounted on vibration isolation supports. In addition, the instruments are placed on top of a high-mass $x$-$y$ movable optical table intended to reduce in the noise the optical measurements generated by the vibration of the test rig.

## 3. Experimental techniques

The flow characterization presented in this study includes the measurement of the air longitudinal velocity, $u_g$, of the particle concentration, $\alpha_p$, and of the particle volume-size distribution function $f(D)$. In addition, long time exposure and instantaneous flow visualizations of the particle flow field were also performed to obtain a global characterization of the particle dispersion process.

The streamwise gas velocity measurements were conducted with a single Pt–10%Rh 2.5 μm diameter hot wire, 1 mm long. The spanwise location of the sensor (58 mm from the lateral wind tunnel wall) was within the droplet-free region close to the wind tunnel sidewall. As a result, the measurements avoided signal contamination due to droplet impingement and lateral boundary-layer interference effects. The hot wire was connected to an AN–1003 AA system amplifier. The resistive overheat ratio was set equal to 0.5. The hot-wire calibration involved a standard least-square approximation procedure (Perry 1982) and was performed at a controlled wind tunnel temperature of $T_0 = 295$ K. In order to keep analogous operating conditions, the experiments were always conducted within the temperature range:

$$293 < T < 297 \text{ K}. \tag{1}$$

Furthermore, to correct for small temperature fluctuations, the calibration curve was multiplied by a linearized correction factor that included the changes in the operating overheat ratio (Bearman 1971).

The long time exposure flow visualization of the particle flow field was performed by illuminating the dispersion layer with a 10 mm thick, collimated plane of light perpendicular to the $(x, y)$-plane passing through the channel centreline. The camera was placed perpendicular to the sheet of light to capture the 90° light scattered by the droplets. For the instantaneous flow visualizations, the continuous light source was replaced by two collimated stroboscopic flash units. The flash pulse duration was set equal to $\frac{1}{8000}$ s and the units were placed such that the entire test section could be visualized simultaneously.

The time-averaged particle concentration ($\alpha_p$) and size distribution function ($f(D)$) were obtained from an analysis of the small-angle forward light scattering of the particles. A 5 mm laser beam was passed across the span, and the attenuation and small-angle diffraction pattern of the light scattered by the particles were recorded with a 2600 HSD Malvern particle sizer (figure 3*b*).

For a spray of spherial non-absorbing spheres with sizes greater than the illuminating light wavelength and concentration sufficiently small so as to avoid multiple scattering effects, analysis of the laser attenuation and diffraction pattern allows the $z$-averaged particle overall concentration and size distribution to be determined (Chein & Chung 1988). The measurement is, therefore, essentially two-dimensional. Furthermore, and because of the sampling rate of the instrument, only time-average measurements were obtained. For the size-distribution measurements, the instrument discretizes the particle diameter range into 15 intervals. Every interval is characterized by a particle diameter value and includes droplets whose diameters are located within $\pm 12\%$ of this central, representative value.

In addition to the time-averaged particle concentration measurements, information related to the instantaneous structure of the particle concentration field, $\alpha_p(t)$, was obtained from an obscuration probe consisting of a single PIN photodiode connected to a low-noise transconductance amplifier. The arrangement was similar to the size-distribution measurements, with a 2 mW He–Ne laser propagating along the $z$-direction and the photodiode measuring the $z$-averaged attenuation of the beam.

For a laser beam of wavelength $\lambda$ propagating along the homogeneous $z$-coordinate in a scattering medium of thickness $L$, the relation between the $z$-averaged particle concentration and the attenuation of the laser beam can be obtained from Beer's law:

$$\ln\frac{I}{I_0} = -\int_0^L \sigma_\lambda(z)\,\mathrm{d}z, \tag{2}$$

where $\sigma_\lambda(z)$ is the medium's scattering and absorption coefficient and $I_0$ and $I$ are the beam intensity measured without and with the medium respectively. When the scattering medium is composed of spherical particles and multiple scattering effects can be neglected, an analytical expression for $\sigma_\lambda(z)$ can be obtained as a function of the particle concentration and the optical properties of the particles. Multiple scattering is important only for large values of the void fraction. Specifically, when the ratio of the mean particle spacing to laser wavelength and the ratio of the mean particle spacing to particle diameter are greater than unity, independent scattering can be assumed (Hottel *et al.* 1970). In this case, the contributions of the different particles to the scattering and absorption coefficients are additive and $\sigma_\lambda(z)$ can be obtained by analysing a single sphere. The scattering coefficient is then given by (Van de Hulst 1957)

$$\sigma_\lambda(z) = \frac{6\alpha_p(z)}{\pi}\int_0^\infty S_\lambda(D)\frac{f(D,z)}{D^3}\,\mathrm{d}D, \tag{3}$$

where $\alpha_p(z)$ is the volume concentration of the dispersed phase at location $z$; $S_\lambda(D)$ is the optical cross-section of a particle with diameter $D$; and $f(D,z)$ is the particle-volume probability density function at location $z$, with the normalization condition given by

$$\int_0^\infty f(D,z)\,\mathrm{d}D = 1. \tag{4}$$

The optical cross-section for non-absorbing substances with an index of refraction $m$, as given by Mie's theory, is (Van de Hulst 1957)

$$S_\lambda(D) = \tfrac{1}{4}\pi D^2\,(2-4/\rho'\sin\rho' + 4/\rho'\,(1-\cos\rho')), \tag{5}$$

where

$$\rho' = 2\pi D/\lambda\,(m-1), \tag{6}$$

is the modified size parameter.

Expression (5) approaches $\frac{1}{2}\pi D^2$ for $\rho' \gg 1$. For example, for water in air, $m = 1.33$, and for a He–Ne laser with $\lambda = 0.6328$ μm (in the red line), the deviation is less than 5% for diameters bigger than

$$D \geqslant 6\ \mu\mathrm{m}. \tag{7}$$

In this case

$$\sigma_\lambda(z) = 3\alpha_p(z)\int_0^\infty \frac{f(D,z)}{D}\,\mathrm{d}D. \tag{8}$$

If we define

$$\tilde{\alpha}_p\tilde{f}(D) = \frac{1}{L}\int_0^L \alpha_p(z)f(D,z)\,\mathrm{d}z, \tag{9}$$

then

$$\ln\frac{I}{I_0} = -3L\tilde{\alpha}_p\int_0^\infty \frac{\tilde{f}(D)}{D}\,\mathrm{d}D, \tag{10}$$

or

$$\tilde{\alpha}_p = \frac{\ln(I_0/I)}{3L\int_0^\infty \tilde{f}(D)/D\,\mathrm{d}D}. \tag{11}$$

With the normalization condition for $f(D,z)$, it follows that

$$\tilde{\alpha}_p = \frac{1}{L}\int_0^L \alpha_p(z)\,\mathrm{d}z, \tag{12}$$

and

$$\tilde{f}(D) = \frac{\int_0^L \alpha_p(z)f(D,z)\,\mathrm{d}z}{\tilde{\alpha}_p L}. \tag{13}$$

From (11), it is seen that the mean concentration along the path is proportional to the logarithm of the ratio of laser intensity with and without spray. Notice also that to compute $\tilde{\alpha}_p$, the volume distribution averaged along the path is needed.

Defining the attenuation function as:

$$\xi = \ln(I_0/I), \tag{14}$$

an expression can be written relating it to $\tilde{\alpha}_p$. Dropping the tilde for magnitudes averaged along $z$, (11) gives

$$\frac{\alpha_p}{\alpha_{p\infty}} = \frac{\int_0^\infty \frac{f(D)}{D}\,\mathrm{d}D\,|_\infty\,\xi_p}{\int_0^\infty \frac{f(D)}{D}\,\mathrm{d}D\,\xi_{p\infty}}, \tag{15}$$

where the subscript $\infty$ refers to some reference state.

Expression (15) reveals the relation existing between the attenuation and the particle concentration functions. Notice that, with respect to the reference state, the attenuation function, $\xi_p/\xi_{p\infty}$, is larger than the particle concentration, $\alpha_p/\alpha_{p\infty}$, for flow regions rich in small-size particulate. A nominal 2 mm laser diameter was employed in the attenuation measurements. The selection of the laser beam diameter for the attenuation measurements was a trade-off between the required spatial resolution and the signal-to-noise ratio needed to keep the error of the measurements below a given level. The main source of noise in these optical measurements resulted from changes in the laser beam orientation due to mechanical vibrations of the test rig. The signals from both the hot wire and the attenuation probes were

| | Mean | R.m.s. | Spec. | Corr. |
|---|---|---|---|---|
| $u_g$ | ±1.5 | ±4.1 | ±12 | $\pm 8\ (\rho = 1)$<br>$\pm 20\ (\rho = 0.2)$ |
| $\alpha_p, \xi$ | ±4.5 | ±5.0 | ±12 | $\pm 8\ (\rho = 1)$<br>$\pm 20\ (\rho = 0.2)$ |
| SMD | ±2.0 | — | — | — |

TABLE 1. Per cent estimated measurement errors for a 95 % confidence interval. The two rightmost columns refer to the spectrum and correlation of the signals respectively. The estimation assumed a 20 % turbulent activity in the mixing layer. The spray indicators were estimated at a point where $\alpha_p = 0.2\alpha_{p\infty}$. The symbol $\rho$ denotes the correlation coefficient.

simultaneously acquired using an A/D converter operating at a 2 KHz sampling rate and producing 16 K words data files. Preconditioning of both signals included linear amplifier circuits to use the A/D converter in its full dynamic range and anti-aliasing passive low-pass filters. The time-averaged concentration and particle-size distribution involved the acquisition of 500 attenuation and diffraction patterns acquired at a sampling rate low enough to ensure statistical independence of each sample.

An estimate of the errors involved in the different measurements is given in table 1. These estimations include both the inherent errors of the techniques and the signal-to-noise ratio of the measurements and the statistical errors associated with the finite length of the records (Lázaro 1989).

## 4. Initial flow conditions

The free-stream velocity for the particle carrier gas was selected to be 15 m $\text{s}^{-1}$. The turbulence level generated by the atomizers in the free-stream air was then an order of magnitude smaller than the ones encountered in the high-Reynolds-number mixing region. In addition, the characteristic particle velocity and acceleration in the mixing layer were much higher than those produced by the gravitational sedimentation (Bachalo & Houser 1984).

The free-stream particle concentration was chosen as a compromise to work in the dilute spray regime while having high attenuation values in the obscuration measurements. In the dilute regime the structure of the carrier gas turbulence is unaffected by the presence of the particles. This situation will occur when the difference between the kinetic energy per unit volume of the particles and that of the carrier air is much smaller than the kinetic energy of the air, i.e.

$$\alpha_p \ll \frac{\rho_g}{\rho_p}\left|\left(\frac{u_p}{u_g}\right)^2 - 1\right| = o(10^{-3}), \qquad (16)$$

where $\alpha_p$ is a characteristic value of the particle concentration and $\rho_p$, $\rho_g$ are the particle and air densities respectively. The order of magnitude for the free-stream particle concentration in the present study was selected to be

$$\alpha_{p\infty} = o(10^{-5}),$$

and therefore satisfies criterion (16).

The characteristics of the cross-stream velocity profiles at $x = 0$ are given in figure 4. The free-stream is characterized by a ±1.2 % inhomogeneity in the mean profile

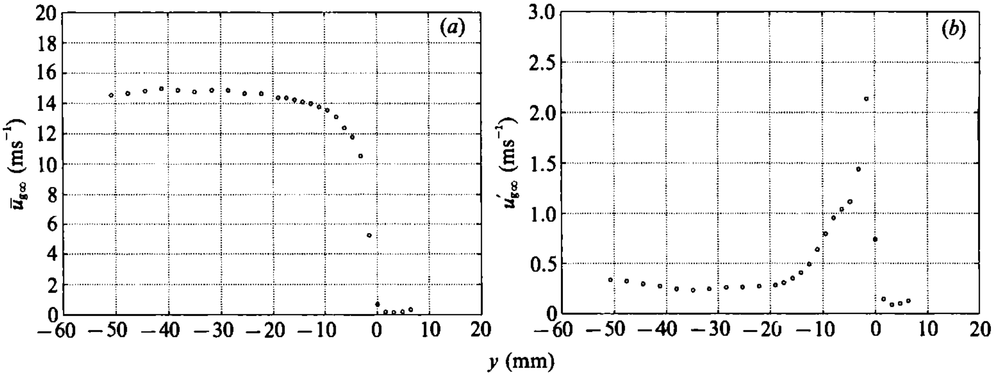

FIGURE 4. Cross-stream gas properties profiles at $x = 0$: (*a*) longitudinal mean velocity, (*b*) longitudinal r.m.s. velocity.

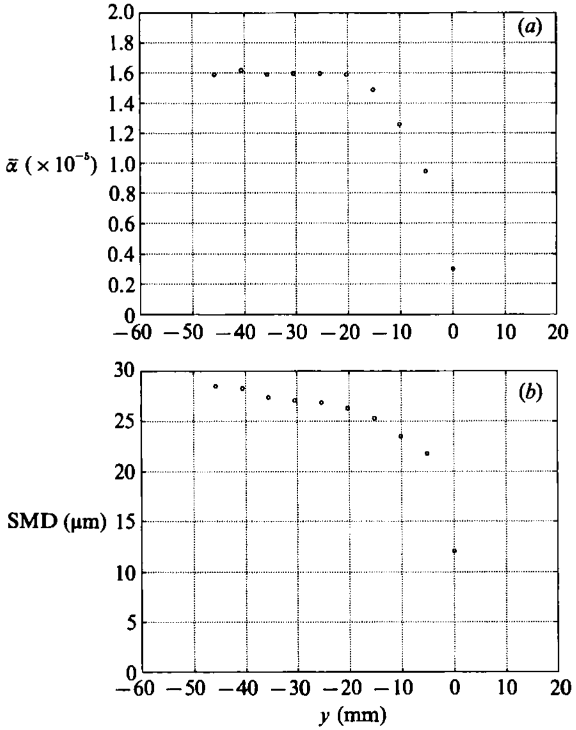

FIGURE 5. Cross-stream spray properties profiles at $x = 0$: (*a*) mean overall particle concentration, (*b*) mean Sauter mean diameter.

and a 1.8% turbulence level. The boundary layer is clearly turbulent, exhibiting a localized peak in the r.m.s. profile and is characterized by a 1.7 mm momentum thickness. In addition, the spanwise profile of the free-stream velocity at $x = 0$ shows that the presence of the atomizers results in only a ±1.2% inhomogeneity along the $z$-coordinate (Lázaro 1989).

The spray cross-stream characteristics at $x = 0$ are shown in figures 5 and 6. For all the experiments reported here, the flow rates of the different rows of atomizers were adjusted to obtain as homogeneous a free-stream particle concentration as

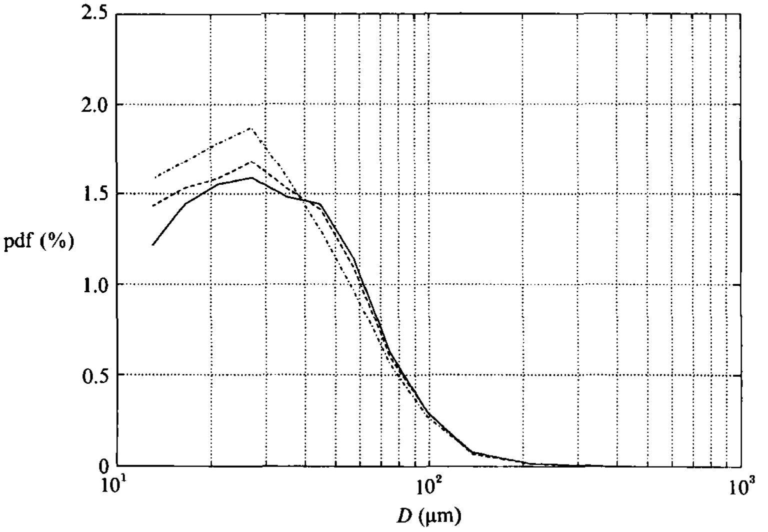

FIGURE 6. Free-stream particle volume-size distribution density function, $x = 0$: ——, $y = -50$ mm; ----, $-40$ mm; —·—·—, $-30$ mm.

possible. The overall mean profile is characterized by a $\pm 0.9\%$ inhomogeneity around an average free-stream value of

$$\bar{\alpha}_{p\infty} = 1.6 \times 10^{-5}. \tag{17}$$

The 90% thickness of the particle-concentration boundary layer at the trailing edge of the splitter plate is 14 mm. In addition, observe that the concentration immediately below the splitter plate, $y = 0$, is $0.2\alpha_{p\infty}$. As a result, there is a strong vertical gradient in particle concentration at $x = 0$, $y = 0$. A commonly used average size to characterize polydispersed sprays is the Sauter mean diameter of the particle distribution:

$$\mathrm{SMD}^{-1} = \int_0^\infty \frac{f(D)}{D} \mathrm{d}D,$$

which represents the size of a monodispersed particulate that would have the same number density and volume-to-area ratio as the actual spray. The cross-stream profile of this variable at $x = 0$ (figure 5*b*) reveals the presence of small particulate in the concentration boundary layer. Gravitational sedimentation effects are strongly felt in this area of reduced longitudinal velocity and long residence times. Notice, in contrast, the small amount of sedimentation present within the free stream, $y < -15$ mm. The free-stream particle volume-size probability density function (p.d.f.) at $x = 0$ is shown in figure 6. Observe that the gravitational effects translate into a slight increase in the small-size p.d.f. percentage in regions close to the splitter plate. The variations, however, are almost within the instrument's detection threshold limit.

With the experimental conditions selected for this study, a quasi-steady analysis of the particle evaporation effects shows that a 10 $\mu$m droplet undergoes a 1% relative size change during the flight time of the particles in the measurement window. The droplet evaporation and the reduction in the carrier gas temperature that occur in the contraction section are sufficient to almost saturate the carrier gas when the spray reaches the trailing edge of the splitter plate. In addition, estimates

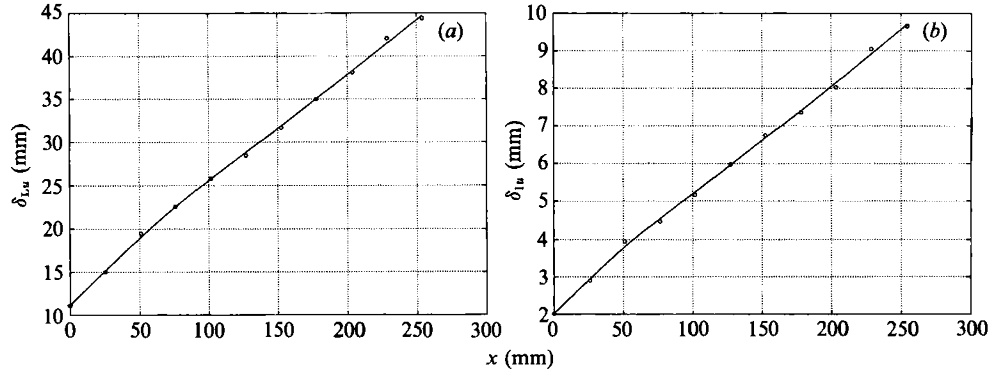

FIGURE 7. Downstream evolution of the longitudinal gas velocity thicknesses: (*a*) 0.1–0.9 level thickness, (*b*) integral (vorticity) thickness.

of the interparticle distance and the particle–gas relative velocities lead to the conclusion that aglomeration and breakup processes as well as multiple scattering effects are negligible throughout the measurement window (Lázaro 1989).

To estimate the effects of particle evaporation, the variation of the free-stream SMD with the downstream location was checked within the measurement window. Inhomogeneities of a random character in the ±3% range were found to exist at the 10 positions measured, mainly produced by irregularities in the atomizers' supply pressure. Therefore, the undisturbed spray is close enough to the saturation state for evaporation effects to play only a secondary role in the dynamics of the particles.

## 5. Gas mixing-layer characterization

Measurements of the mean ($\bar{u}_g$) and r.m.s. ($u'_g$) longitudinal gas velocity cross-stream profiles were performed at 11 equally spaced downstream stations in the range $0 \leqslant x \leqslant 25.4$ cm. From these profiles, quantities defining the lateral spread of longitudinal momentum can be computed. Specifically, two thicknesses will be used:

(*a*) 0.1–0.9 level thickness, $\delta_{Lu}$:

$$\delta_{Lu} = y(\bar{u}_g/\bar{u}_{g\infty} = 0.1) - y(\bar{u}_g/\bar{u}_{g\infty} = 0.9); \tag{18}$$

(*b*) integral (momentum) thickness, $\delta_{Iu}$:

$$\delta_{Iu} = \int_{-\infty}^{\infty} \frac{\bar{u}_g}{\bar{u}_{g\infty}}\left(1 - \frac{\bar{u}_g}{\bar{u}_{g\infty}}\right) \mathrm{d}y. \tag{19}$$

The evolution of these two variables is presented in figure 7. The non-dimensionalizing velocity is taken as the mean velocity in the interval $-50 \leqslant y \leqslant -45$ mm. Note that both thicknesses exhibit an initial nonlinear regime approaching a linear growth. A least-squares fit in the linear region, $x > 10.16$ cm, gives

$$\delta_{Lu} = 1.271 + 0.126x, \tag{20}$$

$$\delta_{Iu} = 0.22 + 0.0294x. \tag{21}$$

The resulting virtual origin of the velocity spreading, i.e. the $x$-location for which expressions (20) and (21) give zero thickness is

$$x_{Lu_0} = -10.0 \text{ cm}, \tag{22}$$

$$x_{Iu_0} = -7.5 \text{ cm}. \tag{23}$$

Because of the turbulent character of the boundary layer emanating from the

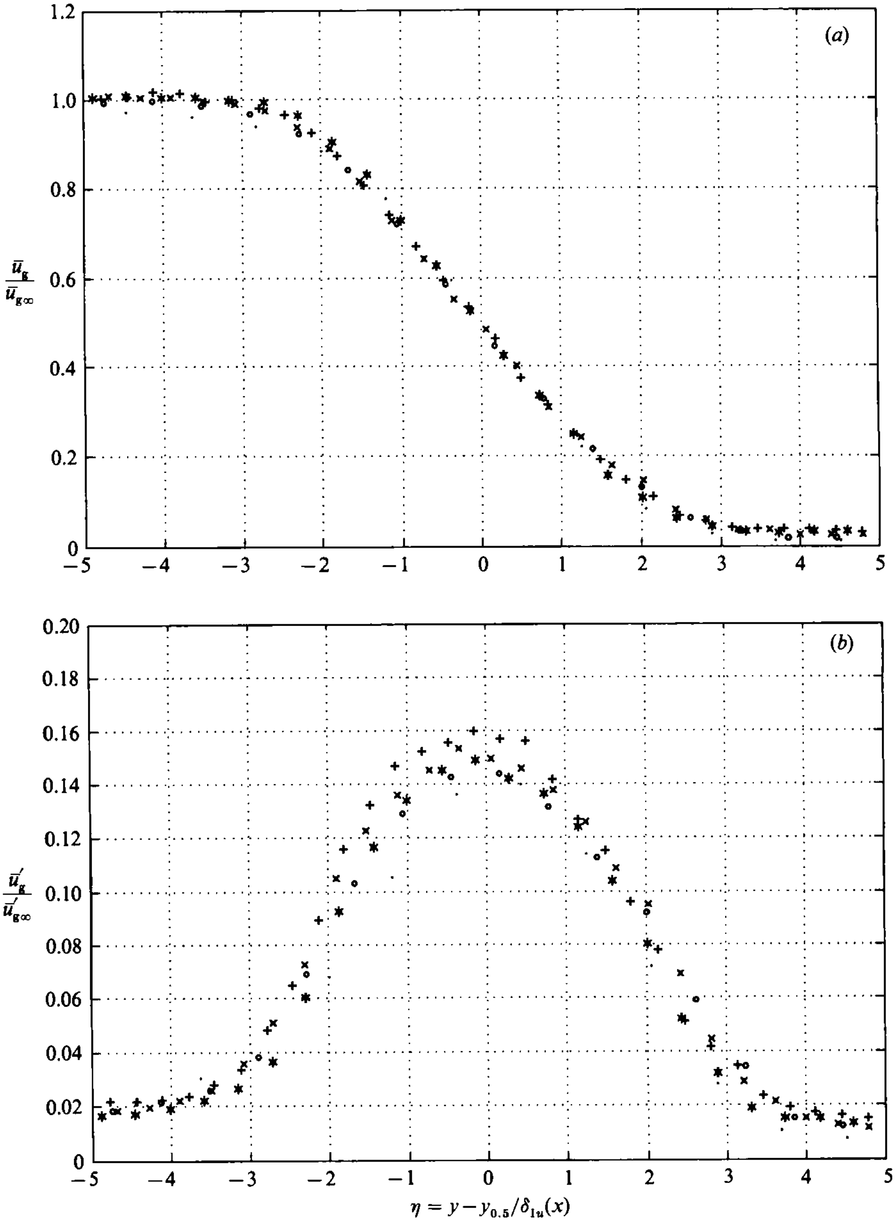

FIGURE 8. Longitudinal gas velocity evolution in similarity coordinates: (a) mean velocity, (b) r.m.s. velocity. ·, $x = 5.1$ cm; ○, 10.2 cm; *, 15.3 cm; ×, 20.3 cm; +, 25.4 cm.

splitter plate, the asymptotic growth rates in the velocity spreading should be achieved between 200 and 400 initial momentum thicknesses (Browand & Latigo 1979; Weisbrot, Einav & Wygnanski 1982). Since the present measurement window spans only 149 initial momentum thicknesses, it is expected that the spreading laws given by expressions (20) and (21) are somewhat smaller than the final values achieved in the asymptotic state.

The evolution of the mean and r.m.s. longitudinal velocity profiles is shown in similarity variables in figure 8. As one should expect from the above remark, the similarity plots reveal the changing condition still existing in the layer. In particular,

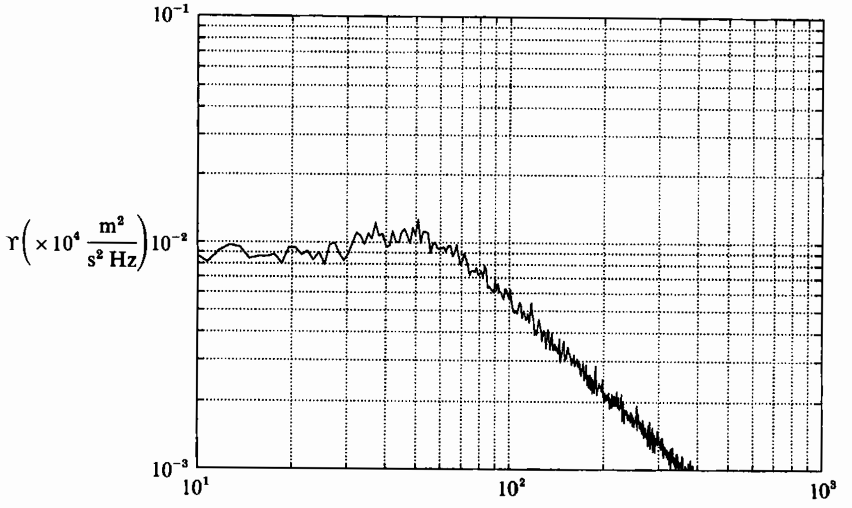

FIGURE 9. Longitudinal gas velocity fluctuation power spectrum, $x = 17.8$ cm, $y = -5$ mm.

note the continuous increase in the peak r.m.s. as one moves downstream. The maximum value attained in the farthest downstream location measured is 16%. Notice, however, that the mean velocity profiles already exhibit a good degree of collapse.

The spectral characteristics of the longitudinal velocity fluctuations within the mixing region (figure 9) show no clear band of preferential frequencies, suggesting the tri-dimensionality present in the developing mixing layer. The high-frequency contents of the spectra can be well adjusted by a power law. In the frequency range $400 < f < 900$ Hz, the best approximating power law gives a negative exponent that increases with the downstream distance, being $-1.40$ at $x/\delta_{\mathrm{I}u_0} = 14$ and $-1.55$ at $x/\delta_{\mathrm{I}u_0} = 143$. An analysis of the spectra of the irrotational fluctuations in the stagnant air region (figure 10), however, reveals the two-dimensional flow structure. The coherent motion appears as a frequency range of enhanced spectral content. The determination of the most amplified frequency, and its evolution with the downstream distance is, however, subject to considerable uncertainty. This is due to the wide range of frequencies showing preferential spectral content and the response of the irrotational gas motion to the turbulent fluctuations of the shear layer, which tends to highlight the larger-scale eddies. When the data at $x/\delta_{\mathrm{I}u_0} = 14$ are corrected for the base-line decay observed at low frequencies, a most-amplified frequency of $f_{\mathrm{max}} = 136$ Hz is obtained, corresponding, with an average convection velocity of $\bar{u}_c = \frac{1}{2}(\bar{u}_{1\infty} + \bar{u}_{2\infty}) = 750 \text{ cm s}^{-1}$, to a wavelength of $\lambda_{\mathrm{max}} = 5.5$ cm. The mixing layer that, according to linear theory, produces such a most-amplified wavelength is characterized by an initial momentum thickness of

$$\delta_{\mathrm{I}u_0} = \frac{\lambda_{\mathrm{max}}}{28.6} = 0.19 \text{ cm}, \tag{24}$$

which agrees well with the calculated initial boundary-layer momentum thickness (0.17 cm for the fast-stream carrier gas).

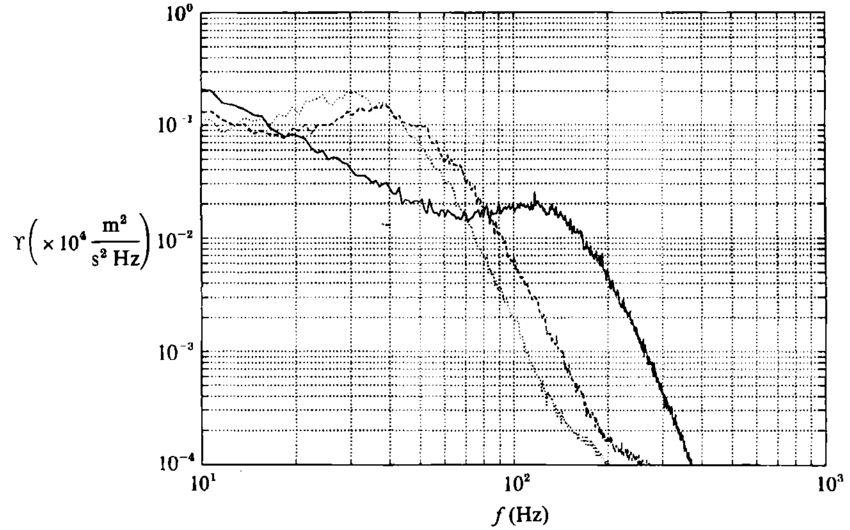

FIGURE 10. Longitudinal gas velocity fluctuation power spectra in the low-speed irrotational region: ——, $x = 2.5$ cm, $y = 2.5$ cm; ----, $x = 17.8$ cm, $y = 5.1$ cm; ......, $x = 25.4$ cm, $y = 6.4$ cm.

## 6. Mean particle dispersion characteristics

A discrete particle dispersed in the plane mixing layer is subjected to a variety of turbulent scales as it flies down from its initial position. Heavy particles released in the fast-stream side of the mixing layer will penetrate a distance in the mixing region before dispersing laterally. The first effect felt by the particles in their interaction with the surrounding gas is a deceleration in their longitudinal velocity as they encounter regions of reduced mean gas velocity $\bar{u}_g$. As the particles are decelerated by the mean flow, they are exposed to the turbulent fluctuations developing in the mixing region. For a turbulent eddy to have a substantial effect on the particle dispersion, two conditions have to be satisfied: ($a$) The eddy-particle relative motion must be characterized by low enough Lagrangian frequencies; and ($b$) the eddy's lifetime must be long enough for the particles to move appreciably before the correlation of the turbulent velocity is lost.

A long-time-exposure photograph of the particle dispersion field is presented in figure 11. This picture shows the time-averaged 90° light scattered by the particles present in the mixing region. The core of the spray (free stream) and the dispersion layer, whose edge is characterized by an initial nonlinear growth, are visible. In addition, it can be observed that the spray spreads mostly towards the stagnant air region (upper darker portion of the figure).

Using non-dimensionalization parameters analogous to the ones employed with the velocity data, figure 12 shows the development of the overall mean particle concentration field with the downstream distance. Because the evaporation effects are negligible throughout the test section in the present experimental conditions, the area under the non-dimensional concentration profile has a constant value, i.e. the integral

$$I = \int_{-40}^{40} \frac{\bar{\alpha}_p}{\bar{\alpha}_{p\infty}}\bigg|_x \,\mathrm{d}y, \tag{25}$$

is within ±2% for all downstream distances.

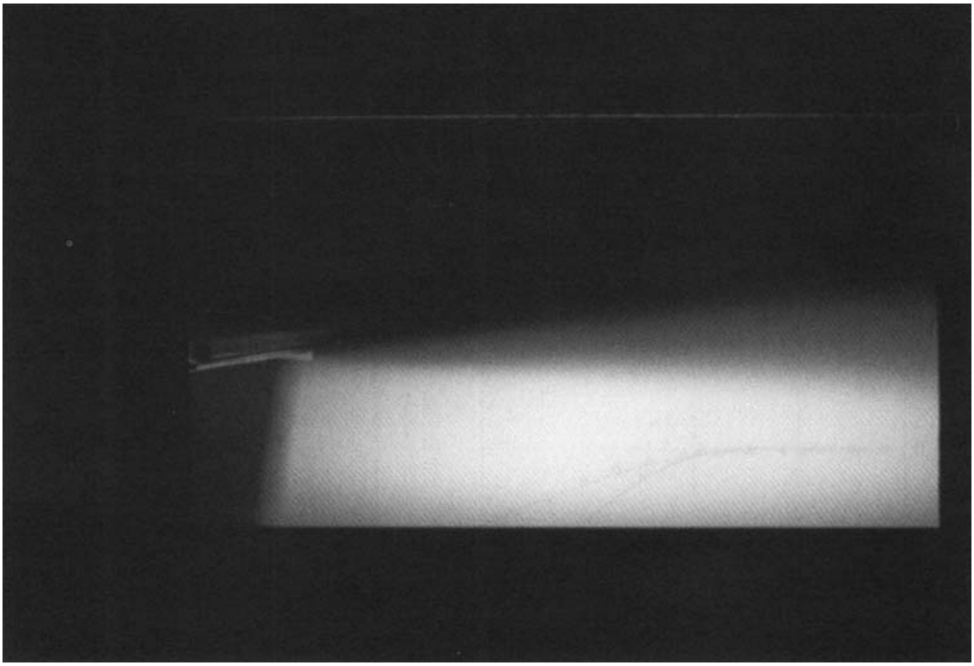

FIGURE 11. Long-time-exposure particle flow visualization. Exposure time: $\frac{1}{2}$ s. Flow is from left to right. Undisturbed spray occupies the lower portion of the photograph. Maximum downstream distance displayed is $x = 25.4$ cm.

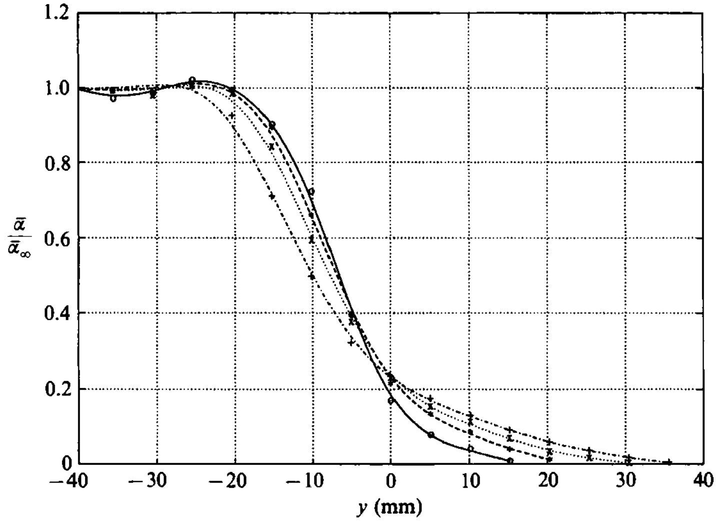

FIGURE 12. Non-dimensional overall cross-stream particle concentration profiles: ○, $x = 10.2$ cm; $*$, 15.2 cm; ×, 20.3 cm; +, 25.4 cm.

A qualitative comparison between the transport of longitudinal momentum and particle concentration is given in figure 13, where the non-dimensional profiles of both quantities at $x = 0$ cm and $x = 20.3$ cm are shown simultaneously. Although the difference in boundary-layer profiles of the $\bar{u}_g$ and $\bar{\alpha}_p$ functions precludes a direct comparison, it can be observed that the extension of the mixing region for the

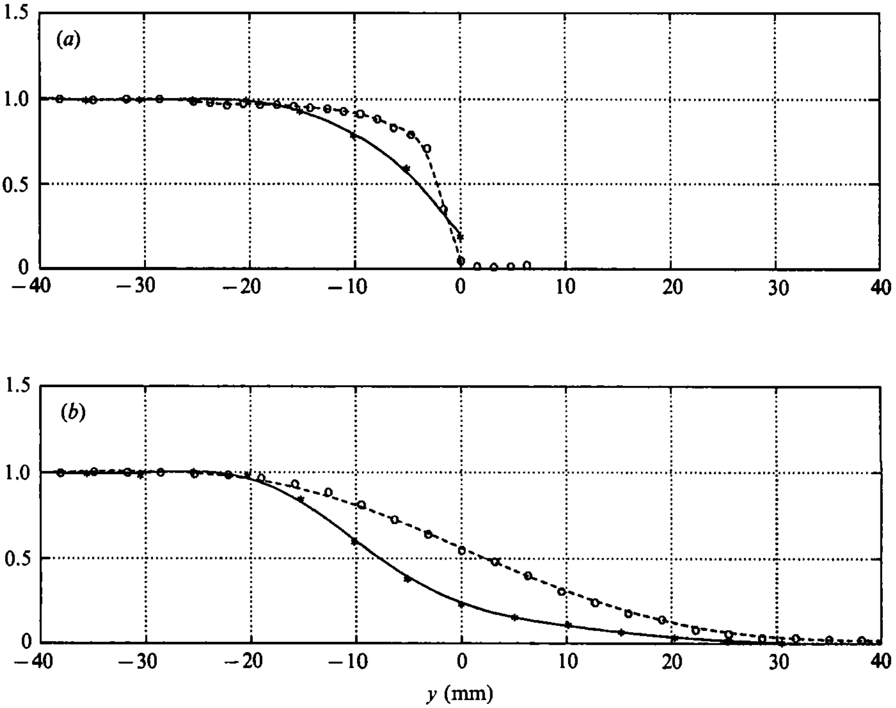

FIGURE 13. Comparison between the mean particle concentration (*) and longitudinal velocity (○) cross-stream profiles: (*a*) $x = 0$ cm; (*b*) $x = 20.3$ cm.

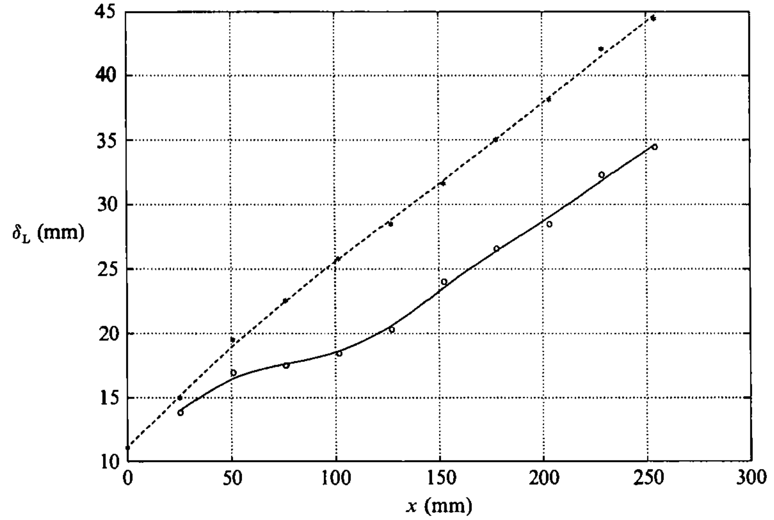

FIGURE 14. Comparison between the downstream evolution of the overall particle concentration (○) and longitudinal gas velocity (*) level thickness.

particle concentration field is lagging well behind that of the velocity. A more definite comparison can be obtained using the spreading rates of the concentration field (figure 14). Three distinct regions can be observed in the evolution of the particle concentration 0.1–0.9 level thickness, $\delta_{L\alpha}$, with each of them characterized by a different sign in their curvature. These three regions are also found in the particle concentration integral thickness, $\delta_{\mathrm{I}\alpha}$, which follows a similar evolution. Near the origin (close to the splitter plate), an area of negative curvature, spanning up to a downstream distance of 5 cm, can be observed. This viscous-like dispersion region is followed by an area with a very slow spreading rate, characterized by a positive curvature. Approximately, the extension of this area reaches up to $x = 15$ cm and is followed by a linear, zero-curvature region.

Considering the particle concentration boundary-layer profile (figure 5), the existence of an initial region with negative curvature in the spreading curve expected. As the concentration value in the lower part of the splitter plate does not have to be zero, an area of high curvature in the concentration profile is located in the region close to the origin of the mixing layer. The turbulent velocity fluctuations associated with the boundary layer, plus the additional relative motion of the still evolving spray give rise to an effective transport of particles wherever there is a concentration gradient.

The second region in the particle dispersion evolution is characterized by a positive curvature in the thickness profiles. This behaviour contrasts with the evolution of the velocity thickness and is a characteristic of the initial transport process of discrete particles. This area can be thought of as an induction region, in which the spreading rate grows from an almost zero value to the final one characterizing the linear spread. Moreover, the extension of this region is directly responsible for the reduced values that the particle thicknesses show when compared with their counterparts in the longitudinal gas momentum field. The induction region ends when the growth rate of the concentration thickness stabilizes to reach a constant value. Although because of the experimental uncertainty, it is difficult to fully ascertain the extension of region II, the curvature changes downstream of the location $x = 15$ cm appear to be practically negligible.

In region III the particulate spreads in a linear fashion, similar to what occurs with the longitudinal gas momentum. A least-squares fit of the data corresponding to this asymptotic region, $15.24 < x < 25.4$ cm, gives

$$\delta_{\mathrm{L}\alpha} = 7.84+0.105x, \tag{26}$$

$$\delta_{\mathrm{I}\alpha} = 1.96+0.0215x. \tag{27}$$

## 7. The mean particle-size distribution field

A very important aspect in the dispersion of particulates by anisotropic turbulence is the investigation of the role that the particle size may play in the extension and characteristics of the mixing region. The ratio of drag to inertial forces acting on a particle of sufficiently small size is inversely proportional to the square of its diameter. Therefore, it follows that in the limit of very small particles, $D \rightarrow 0$, the drag mechanism is so effective that the relative motion between the particle and the gas has to vanish if the accelation of the particle is to remain bounded.

Consequently, in this limit and in the case of dilute suspensions, the particles will behave like a passive scalar. If, in addition, evaporation effects are not present and the particles are not so small that molecular collisions impart momentum changes to them, their dispersion will be produced entirely by turbulent effects. At the other extreme, particles for which the ratio of inertial to drag forces is large will hardly be dispersed by the turbulence because the turbulence–particle momentum transfer mechanism is ineffective in modifying their acceleration. Between these two limits, there is a range of diameters that will be partially affected by the turbulence. The

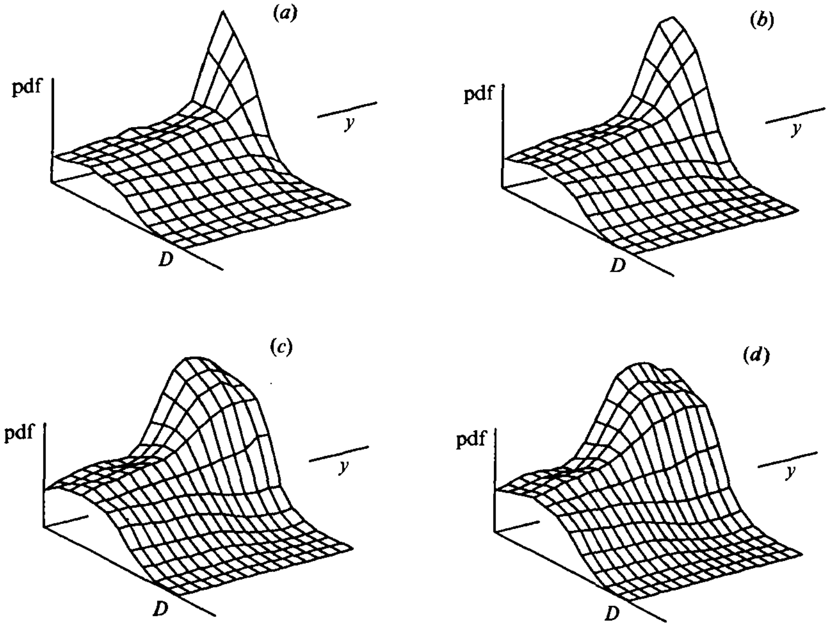

FIGURE 15. Downstream evolution of the particle volume-size pdf: (a) $x = 7.6$ cm, (b) $x = 12.7$ cm, (c) $x = 20.3$ cm, (d) $x = 25.4$ cm. Surfaces represent the functions $\mathrm{pdf} = \mathrm{pdf}(y, D)|_{x=\mathrm{constant}}$.

spatial changes of the turbulent characteristics in inhomogeneous flows implies that the dispersion of a marked particle will depend not only on its present position, but also on its history. The way in which the size may affect this history will also lead to distinctive dispersion properties of the particulate.

A suitable variable for characterizing the size effects in the discrete particle dispersion problem is the volume-size probability density function of the particle concentration which gives information about the concentration of the different particle sizes along the mixing region.

The evolution of this function with the downstream distance is given in figure 15, where its cross-stream variation has been plotted for several downstream locations. The first observation one can make from these p.d.f. surfaces is the strong inhomogeneity encountered in the mixing region, located in the rightmost area of each plot. This inhomogeneity is characterized by a dramatic increase in the percentage of the p.d.f. corresponding to the small particles across the dispersion layer. At each downstream location, therefore, the dispersion region close to the undisturbed spray has a p.d.f. with a higher percentage of small particulate. It can then be said that the dispersion is occurring as a size-selective process.

To evaluate the changes in the p.d.f. percentage of different particle sizes, cross-stream variations with respect to the undisturbed, free-stream value are calculated according to

$$\Delta(D, x, y) = \frac{\mathrm{pdf}(D, x, y)}{\mathrm{pdf}(D, x, -\infty)} - 1. \tag{28}$$

At each downstream location, this function will have positive values for those diameters transported more efficiently into the mixing layer and negative ones for those sizes that show, within the dispersion layer, a decrease in the p.d.f. percentage. The evolution of this function for the discretized size groups represented by average

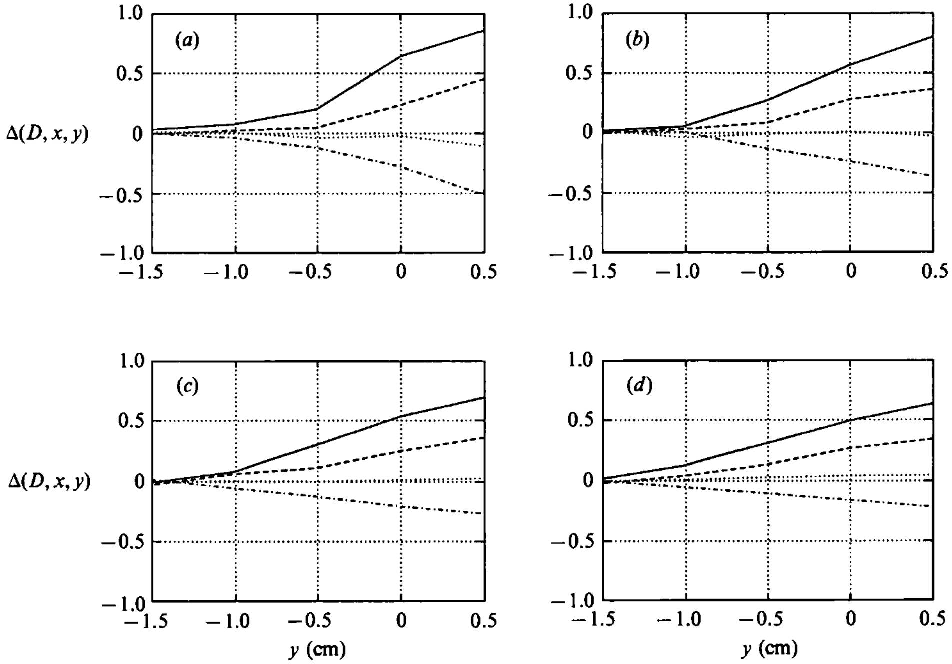

FIGURE 16. Downstream evolution of the incremental relative pdf, $\Delta(D,x,y) = [\mathrm{pdf}(D,x,y)/\mathrm{pdf}(D,x,-\infty)]-1$ for four different particle size groups: (a) $x = 10.2$ cm, (b) $x = 15.2$ cm, (c) $x = 20.3$ cm, (d) $x = 25.4$ cm. ——, $\bar{D} = 16.5$ µm; ---, 21.1 µm; ....., 27.0 µm; —·—·—, 34.8 µm.

diameters equal to 16.5, 21.1, 27.0, and 34.8 µm is shown in figure 16. As one would expect, the small droplets (16.5 and 21.1 µm) show a positive value of $\Delta(D,x,y)|_x$ whereas the group of larger size droplets (34.8 µm) shows a negative $\Delta$ in all the downstream positions measured. Notice that the 27.0 µm group has a negative variation for $x = 10.2$ cm which becomes positive farther downstream at $x = 25.4$ cm.

The probability density functions of figure 15 show that, in the outer portion of the dispersion layer, the small-particulate selection mechanism reaches a stabilization and is even slightly reversed when the farthest downstream locations are analysed. To stress this aspect, the cross-stream p.d.f. variations at $x = 25.4$ µm for two widely separated diameter ranges have been plotted in figure 17. The selected droplet groups have average diameters of 13.0 and 57.4 µm. The p.d.f. percentages have been made dimensionless with their farthest free-stream values. It can be observed that the selective process occurring when entering the dispersion layer remains active until a cross-stream position of approximately $y = 15$ mm is reached. From there on, a relative decrease in the small sizes and the associated increase in the large ones is seen to occur.

In conclusion, as we move from the undisturbed spray mixing layer, the dispersion region is characterized first by an internal layer where a progressive accumulation of small droplets occurs, followed by an external sublayer where a slight increase in the concentration of large droplets takes place.

The small-size selective mechanism will ultimately lead to a depletion of small-diameter particulate in the regions close to the inner edge of the dispersion layer. When the amount of dispersed small particulate is sufficiently large, a new sublayer

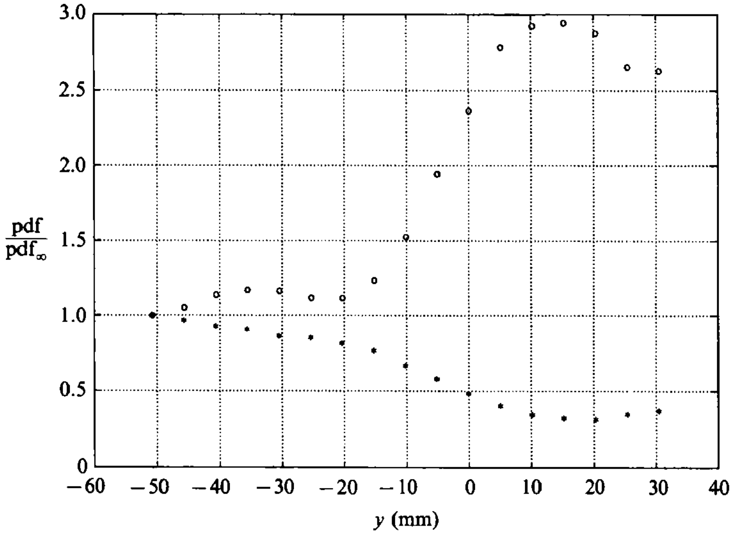

FIGURE 17. Cross-stream non-dimensional p.d.f. profiles for particle-size family groups $\bar{D} =$ 13.0 μm (○) and $\bar{D} = 57.4$ μm (*) at $x = 25.4$ cm. Non-dimensionalizing p.d.f. is the corresponding one for each family group at $y = -50$ mm.

in the p.d.f. surfaces will form at the inner edge of the dispersion region. This effect is seen in figure 17 for the very small droplets. Unfortunately, at this downstream location, the effects of gravitational settling are of a similar order of magnitude and opposite, thus masking the above-mentioned mechanism. A careful analysis of the data in figure 17 reveals the gravity sedimentation effect present in the free-stream spray. Between $-50 \leqslant y \leqslant -30$ mm the small particulate slightly increases its percentage and the larger size one is decreased, revealing the occurring sedimentation process. Between $y = -30$ and $-20$ mm (the approximate inner edge of the dispersion layer), the small droplets have a local decrease in the p.d.f. percentage level whereas, although hardly noticeable at this stage, the large-diameter group experiences a local stabilization in its continuous decay towards its outermost value. This process eventually leads to the emergence of a second, inner sublayer, also characterized by a local accumulation of large-size droplets.

The observations discussed above are consistent with the analysis of mean diameters of the distribution, calculated from the probability density functions. Figure 18 shows cross-stream profiles of the Sauter mean diameter (SMD) for downstream locations $x = 5.1$, 17.8, and 25.4 cm. The profiles have been made dimensionless with the average SMD measured between $-50 < y < -30$ mm. Observe how in the core of the dispersion layer the selection process results in reductions of the SMD to half its free-stream value. The minimum is located at about $y = 15$ mm and its value increases with the downstream distance. The presence of the external sublayer is also apparent in these measurements, with the SMD increasing almost linearly in this region. In the core of the spray, the gravitational sedimentation results in SMD changes of about 5% in the cross-stream-coordinate range $-40 < y < -20$ mm. In addition, the SMD-profiles also show the development of the inner sublayer, located around $y = -20$ mm at $x = 25.4$ cm.

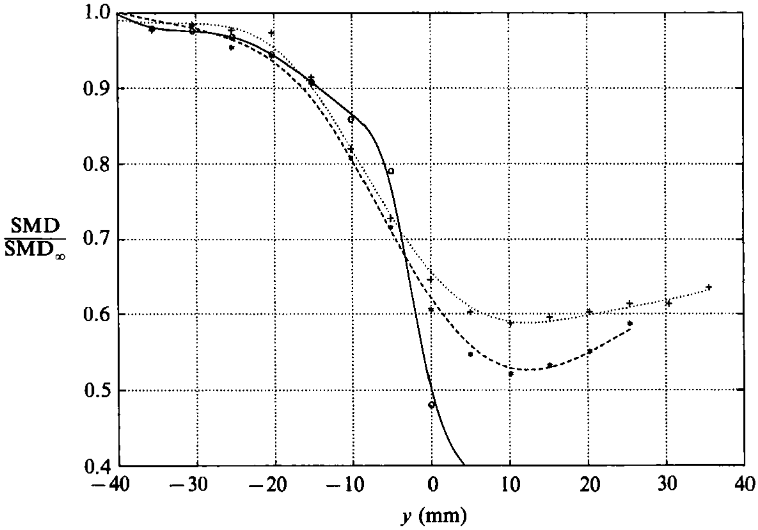

FIGURE 18. Cross-steam profiles of the mean Sauter mean diameter at different downstream locations. Non-dimensionalization size $\mathrm{SMD}_\infty = 27.3\ \mu\mathrm{m}$. ○, $x = 5.1$ cm; $*$, 17.8 cm; $+$, 25.4 cm.

## 8. The dependence of the dispersion properties on the particle size

In §7 the acute inhomogeneities that the particle volume-size p.d.f. possesses across the dispersion layer were demonstrated. This information hints at the strong influence that size has on the dispersion characteristics of discrete particles. The p.d.f. percentage distribution and the overall spray concentration are the data necessary to compute the concentration of the different droplet family groups, thus allowing a parametric study of the dependence of the dispersion properties upon the particle size.

A typical set of cross-stream concentration profiles for several droplet diameters and a given downstream location is shown in figure 19. Consistent with the p.d.f. surfaces shown in figure 15, these profiles reveal the strong dependence of the spreading rates upon the particle size, with the maximum spreading corresponding to the mean concentration profiles of the small particulate. Similarly to what was done with the velocity and the overall concentration data, the mean profiles of the particle group concentrations can be used to measure the 0.1–0.9 level thickness ($\delta_{L\alpha}(D)$) and integral thickness ($\delta_{I\alpha}(D)$) characterizing the spreading rate of each size family.

The downstream evolution of the 0.1–0.9 level thickness for four representative particle groups is given in figure 20. As a comparison, the corresponding evolution of the velocity thickness is also shown in the figure. The conclusion that can be extracted from these data is that the evolution of each droplet size family shows the same trends observed in the overall concentration data given in figure 14, namely, the existence of an initial induction region, characterized by a positive curvature, followed by an asymptotic linear growth region. Moreover, the extension of the induction region is found to scale with the droplet diameter, increasing with it. On the other hand, notice that the asymptotic state of the linear growth seems to be size independent, reaching the value characterizing the spreading of momentum, a result which is known to hold for homogeneous turbulence (Hinze 1975).

After noticing the strong influence that the particle diameter has on the dispersion evolution, it is important to search for a non-dimensionalization that can render size-

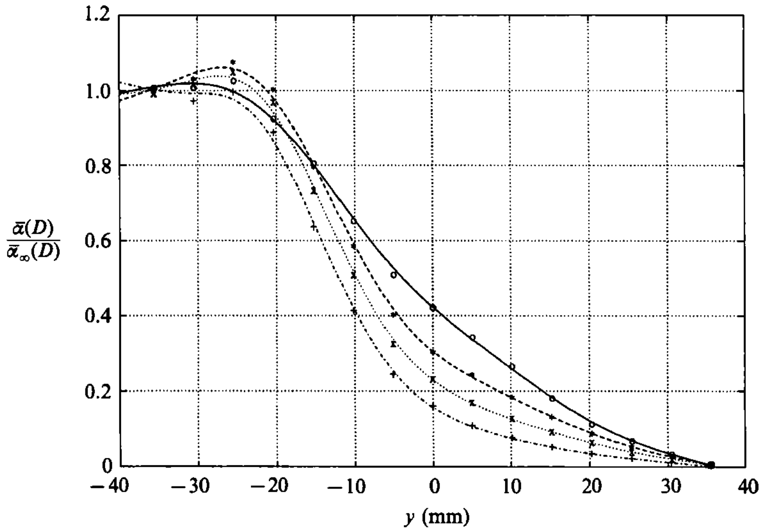

FIGURE 19. Cross-stream profiles of the mean non-dimensional particle concentration for different particle family groups, $x = 25.4$ cm. ○, $\bar{D} = 16.5$ µm; *, 27.0 µm; ×, 34.8 µm; 44.6 µm.

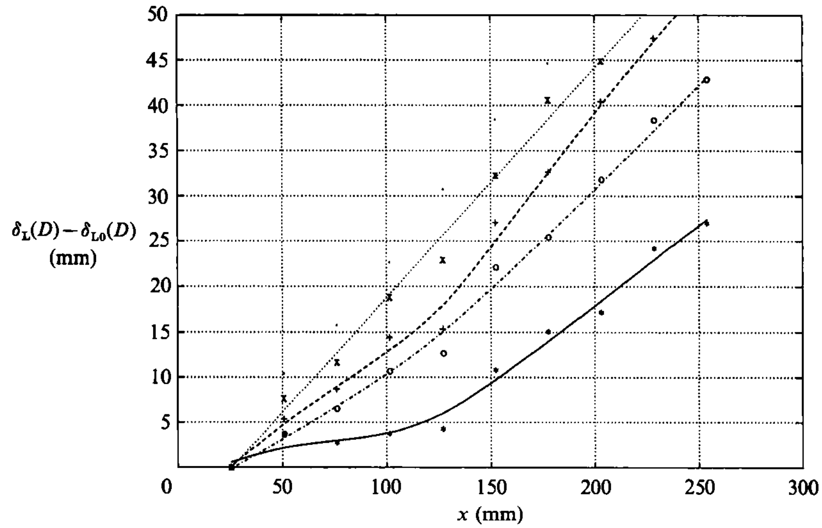

FIGURE 20. Downstream evolution of the 0.1–0.9 particle concentration level thickness for different size groups. ·, Gas velocity; ×, $\bar{D} = 16.5$ µm; +, 27.0 µm; ○, 34.8 µm; *, 44.6 µm.

independent dispersion properties. The proper non-dimensionalizing scale for this must be obtained from the equation governing the dynamics of the particles. The general expression for the evolution of the particle acceleration includes the unsteady effects and terms originated from the spatial inhomogeneity of the far-field gas velocity seen by the particles (Maxey & Riley 1983).

For the dilute system analysed here, it has been shown that the drag is the leading mechanism in the particle–turbulence momentum transfer (Bachalo & Houser 1984). The motion of the droplets is then given by

$$\mathrm{d}\boldsymbol{u}_\mathrm{p}/\mathrm{d}t + F_1 \boldsymbol{u}_\mathrm{p} = F_1 \boldsymbol{u}_\mathrm{g}, \tag{29}$$

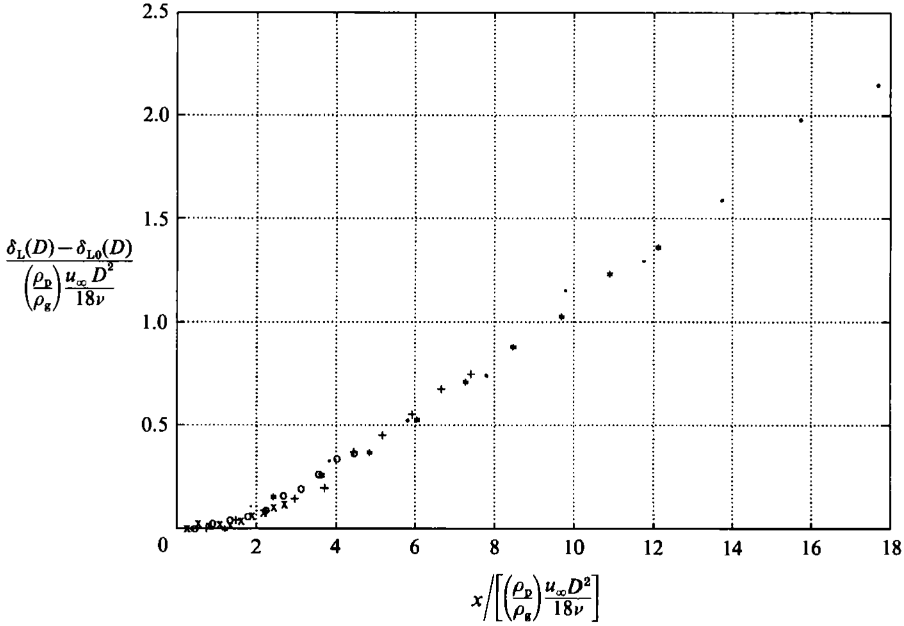

FIGURE 21. Universal particle level thickness evolution curve. ·, $\bar{D}$ = 16.5 μm; ✱, 21.1 μm; +, 27.0 μm; ○, 34.8 μm; ×, 44.6 μm.

where $F_1$ is related to the drag coefficient of the particles, a function of the particle diameter and of the particle–gas relative velocity. For particle sizes and relative velocities falling in the Stokes regime, $F_1$ is a function of the droplet diameter only:

$$F_1 = 18\rho_g/\rho_p \nu D^2, \tag{30}$$

with $\nu$ being the kinematic viscosity of the gas medium. This parameter is the inverse of the particles' Stokes time and represents the characteristic time of the response of the droplets to a step change in the velocity of the surrounding gas. Alternatively, $F_1$ can be interpreted as an upper measure of the frequencies that the particles will be able to track in a turbulent flow field. The Fourier transform of (29) then shows that the particles behave as a first-order system, tracking velocity fluctuations up to a frequency proportional to $F_1$ (Hjemfelt & Mockros 1966). The lengthscale related to the response of the particles to turbulent fluctuations is then the wavelength associated to this cutoff frequency. Choosing $u_\infty$ as a characteristic velocity scale, it follows that

$$L_D = \left(\frac{\rho_p}{\rho_g}\right)\frac{u_\infty D^2}{18\nu}. \tag{31}$$

In order to obtain an asymptotic particle-size-independent thickness growth rate, both lengths $x$ and $\delta$ must be made dimensionless with $L_D$. Physically one can think that the characteristic transversal scales of the turbulence increase with the downstream distance and, therefore, a similar scaling should be made in both variables. The resulting non-dimensional evolution of $\delta_{L\alpha}$, $\delta_{I\alpha}$ is shown in figures 21 and 22. To account for the effect associated with the initial boundary-layer profile, the corresponding thickness at $x = 2.54$ cm has been subtracted in the different data sets.

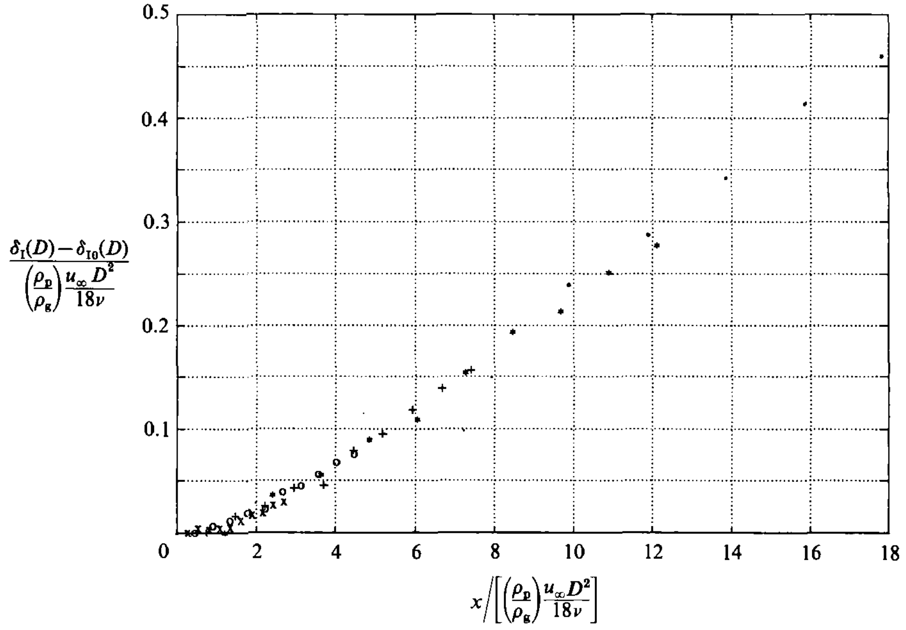

FIGURE 22. Universal particle integral thickness evolution curve. ·, $\bar{D} = 16.5$ μm; $*\bar{D}$, 21.1 μm; +, 27.0 μm; ○, 34.8 μm; ×, 44.6 μm.

As can be seen, both for $\delta_{L\alpha}$ and $\delta_{I\alpha}$ the data collapse fairly well onto a single curve. The large particles with their longer induction lengths show the presence of the initial nonlinear region. Observe that for the $\bar{D} = 44.6$ μm particle size group, almost the entire test section is occupied by the induction region. The asymptotic straight line intersects the $\delta = 0$ axis at

$$x/L_D = 2.19, \tag{32}$$

for the level thickness, and at

$$x/L_D = 2.58, \tag{33}$$

for the integral thickness.

The ability to describe the universal behaviour of $\delta_{L\alpha}(D)$ and $\delta_{I\alpha}(D)$ poses the question whether the non-dimensionalization of the downstream and cross-stream coordinates will produce the collapse not only of the concentration thicknesses, but also of the entire particle family concentration profile. Heuristically, one must recognize that a complete universality is impossible, for the boundary conditions as given by the concentration profiles at $x = 0$ will, in general, not collapse under the present non-dimensionalization. Therefore, there must be an initial region in which the memory of the initial concentration profiles has to be felt. Consequently, further downstream one must expect a better collapse.

To compare the concentration profiles of two different particle families, $D_1$ and $D_2$, the downstream locations must be selected such that

$$x_1/L_{D_1} = x_2/L_{D_2}. \tag{34}$$

Using the above condition, four representative concentration profiles in the non-dimensionalized cross-stream coordinate $y/L_D$ are shown in figure 23. The results have been numbered with increasing value of $x/L_D$. Considering the differences in boundary-layer concentration profiles, test cases (*a*), (*c*) and (*d*) give a very good degree of collapse. In test case (*b*), the data for $\bar{D} = 21.1$ μm deviates from the trend

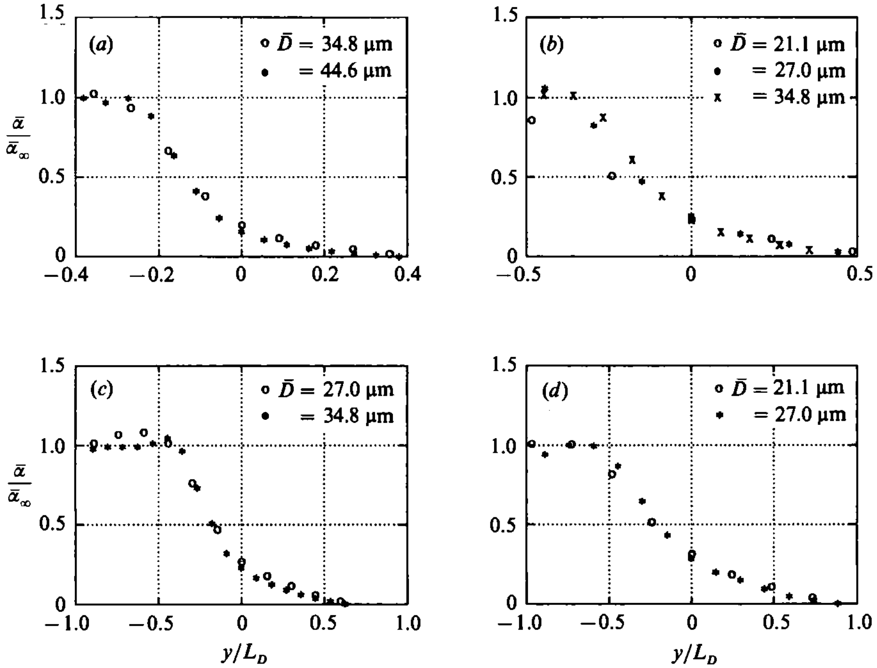

FIGURE 23. Universality of the particle size family concentration profile: (*a*) $x/L_D = 2.71$, (*b*) $x/L_D = 3.56$, (*c*) $x/L_D = 4.45$, (*d*) $x/L_D = 5.92$.

given by the other two family groups for negative values of $y/L_D$. This is not surprising since for this droplet family the non-dimensional parameter $x/L_D = 3.56$ corresponds to a downstream distance $x = 7.6$ cm where the memory of the initial boundary-layer profile is still present. Notice, however, how the data in the dispersion region follow the profile given by the other two particle groups, which correspond to larger downstream locations and are further away from the region where the initial conditions are felt.

A theoretical basis for the above non-dimensionalization can be obtained from the continuum formulation of the particle dispersion field. In this approach, the particles are treated as a continuum characterized by a local concentration $\alpha_\mathrm{p}$ and velocity $\boldsymbol{u}_\mathrm{p}$. These quantities are obtained by performing a spatial average over the particles contained in an elemental volume which is much smaller than the relevant flow scale and which contains enough particles to provide a continuous character to the field variables. The evolution equations for the continuum particle concentration and velocity are then obtained from conservation arguments applied to the elemental volume (Drew 1983). Assuming, as corresponds to our experimental conditions, that the particle–particle interaction and evaporation effects are negligible and that the particles are small enough for the drag term to be the leading mechanism in the particle–gas momentum exchange, the evolution of the field variables is given by

$$\partial \boldsymbol{u}_\mathrm{p}/\partial t + \boldsymbol{u}_\mathrm{p}\cdot\nabla\boldsymbol{u}_\mathrm{p} = F_1(\boldsymbol{u}_\mathrm{g} - \boldsymbol{u}_\mathrm{p}), \tag{35}$$

$$\partial \alpha_\mathrm{p}/\partial t + \nabla\cdot(\alpha_\mathrm{p}\boldsymbol{u}_\mathrm{p}) = 0, \tag{36}$$

where $F_1$ is again related to the drag coefficient acting on a single particle. When the particles and relative velocities are small enough for the Stokes regime to apply, $F_1$ is given by (30).

The evolution of the mean velocity field is obtained by averaging equation (35). For the present two-dimensional flow ($z$-homogeneity), the mean flow is described by

$$U_p \partial U_p/\partial x + V_p \partial U_p/\partial y + F_1 U_p = F_1 U_g - \partial/\partial x\,(\overline{u_p^2}) - \partial/\partial y\,(\overline{u_p v_p}), \tag{37}$$

$$U_p \partial V_p/\partial x + V_p \partial V_p/\partial y + F_1 V_p = F_1 V_g - \partial/\partial x\,(\overline{u_p v_p}) - \partial/\partial y\,(\overline{v_p^2}). \tag{38}$$

In order for the problem to possess size similarity, (37) and (38) have to be non-dimensionalized in such a way that the factor $F_1$ drops out. The only way to achieve this goal is to make the characteristic time of the non-dimensionalization proportional to $F_1^{-1}$. Since a characteristic velocity is given by $\bar{u}_{g\infty}$, this implies that the characteristic length must also be proportional to $F_1^{-1}$.

Therefore, the desired non-dimensionalization is

$$U^* = U/\bar{u}_{g\infty}, \quad V^* = V/\bar{u}_{g\infty}, \quad u^* = u/\bar{u}_{g\infty}, \quad v^* = v/\bar{u}_{g\infty}, \tag{39}$$

$$x^* = \frac{x}{\bar{u}_{g\infty} D^2/18(\rho_g/\rho_p)\,\nu}, \quad y^* = \frac{y}{\bar{u}_{g\infty} D^2/18(\rho_g/\rho_p)\,\nu}. \tag{40}$$

As a consequence, the mean continuum equations determine the lengthscale necessary to ensure size-independent dispersion evolution.

With the non-dimensionalization given by (39) and (40), and dropping the asterisks in the notation, it follows that

$$U_p \partial U_p/\partial x + V_p \partial U_p/\partial y + U_p = U_g - \partial/\partial x\,(\overline{u_p^2}) - \partial/\partial y\,(\overline{u_p v_p}), \tag{41}$$

$$U_p \partial V_p/\partial x + V_p \partial V_p/\partial y + V_p = V_g - \partial/\partial x\,(\overline{u_p v_p}) - \partial/\partial y\,(\overline{v_p^2}). \tag{42}$$

If $o(\overline{u_p^2}) = o(\overline{v_p^2}) = o(\overline{u_p v_p})$ and the thin-layer approximation applies,

$$\partial/\partial y \gg \partial/\partial x, \tag{43}$$

then, (41) and (42) become

$$U_p \partial U_p/\partial x + V_p \partial U_p/\partial y + U_p = U_g - \partial/\partial y\,(\overline{u_p v_p}), \tag{44}$$

$$U_p \partial V_p/\partial x + V_p \partial V_p/\partial y + V_p = V_g - \partial/\partial y\,(\overline{v_p^2}). \tag{45}$$

Notice that, from (40), in the limit $D \rightarrow 0$

$$\partial/\partial x = \partial/\partial y = 0, \tag{46}$$

which gives

$$U_p = U_g, \tag{47}$$

$$V_p = V_g, \tag{48}$$

i.e. the motions of gas and particles are identical.

In general, we will have

$$U_g = U_g(x_R, y_R), \tag{49}$$

$$V_g = V_g(x_R, y_R), \tag{50}$$

with $x_R, y_R$ being the real non-dimensionalized coordinates. If (44) and (45) are to render size-independent results,

$$U_g = U_g(x, y), \tag{51}$$

$$V_g = V_g(x, y). \tag{52}$$

must be satisfied. Since $y_R/x_R = y/x$, the only way to make (49), (50) and (51), (52) compatible is

$$U_g = U_g(y_R/x_R), \tag{53}$$

$$V_g = V_g(y_R/x_R), \tag{54}$$

i.e. similarity in the mean motion of the gas. This is only observed occurring in the fully developed flow. However, as shown in the data presented in figures 7(*b*) and 8(*a*), (53) and (54) describe to a great degree the evolution of the mean gas velocity. Nevertheless, in the developing region, the size similarity can only be approximate. Also notice that it seems reasonable to assume that

$$\overline{u_\mathrm{p} v_\mathrm{p}} = f_1(x, y), \tag{55}$$

$$\overline{v_\mathrm{p}^2} = f_2(x, y), \tag{56}$$

or, in real variables,

$$\overline{u_\mathrm{pR}\, v_\mathrm{pR}} = \bar{u}^2_{\mathrm{g}\infty} f_2\left(\frac{x}{\bar{u}_{\mathrm{g}\infty} D^2/18(\rho_\mathrm{g}/\rho_\mathrm{p})\,\nu}, \frac{y}{\bar{u}_{\mathrm{g}\infty} D^2/18(\rho_\mathrm{g}/\rho_\mathrm{p})\,\nu}\right), \tag{57}$$

$$\overline{v^2_\mathrm{pR}} = \bar{u}^2_{\mathrm{g}\infty} f_2\left(\frac{x}{\bar{u}_{\mathrm{g}\infty} D^2/18(\rho_\mathrm{g}/\rho_\mathrm{p})\,\nu}, \frac{y}{\bar{u}_{\mathrm{g}\infty} D^2/18(\rho_\mathrm{g}/\rho_\mathrm{p})\,\nu}\right). \tag{58}$$

Arguments in favour of (57) and (58) can be conducted from particle spectral response considerations. However, this dependence is not straightforward. In particular, if one considers the governing equation for a single particle

$$\mathrm{d}\boldsymbol{u}_\mathrm{p}/\mathrm{d}t = F_1(\boldsymbol{u}_\mathrm{g} - \boldsymbol{u}_\mathrm{p}), \tag{59}$$

one sees that the acceleration of the particle depends upon its relative velocity with respect to the gas. Therefore there must be dependence of the particle momentum turbulent transport terms, (57) and (58), upon the difference in mean relative motion, at least for the dispersion induced by the large scale. If

$$\overline{u_\mathrm{p} v_\mathrm{p}} = f_1(x, y, U_\mathrm{p} - U_\mathrm{g}, V_\mathrm{p} - V_\mathrm{g}), \tag{60}$$

$$\overline{v_\mathrm{p}^2} = f_2(x, y, U_\mathrm{p} - U_\mathrm{g}, V_\mathrm{p} - V_\mathrm{g}), \tag{61}$$

the differential equations for the particle velocity field (44) and (45) are size-independent.

The equation for the mean particle concentration in non-dimensional form is

$$\frac{\partial(\bar{\alpha}_\mathrm{p} U_\mathrm{p} + \overline{\alpha_\mathrm{p} u_\mathrm{p}})}{\partial x} + \frac{\partial(\bar{\alpha}_\mathrm{p} V_\mathrm{p} + \overline{\alpha_\mathrm{p} v_\mathrm{p}})}{\partial y} = 0, \tag{62}$$

also particle-diameter independent when the main spatial dependence of the particle turbulent transport terms is similar to (60) and (61).

Finally, a full analogy will be found if there is similarity in boundary conditions which satisfies

$$U_\mathrm{p}(0, y_\mathrm{R}, D) = \bar{u}_{\mathrm{g}\infty}\, g_1(y_\mathrm{R}/L_D), \tag{63}$$

$$\bar{\alpha}_\mathrm{p}(0, y_\mathrm{R}, D) = \bar{\alpha}_{p\infty}\, g_2(y_\mathrm{R}/L_D). \tag{64}$$

In general, these conditions will not be satisfied. Therefore, a distance from the beginning of the dispersion must be allowed for the effect of the initial velocity and concentration boundary-layers profiles to be forgotten.

## 9. Temporal structure of the particle field

The most remarkable characteristic of the instantaneous flash-pulse particle flow visualization is the streak pattern that can be identified in the dispersion layer shown in figure 24. These streaks appear in the flow visualization as thin white bands of particles that originate in the core of the spray and whose axes form a small,

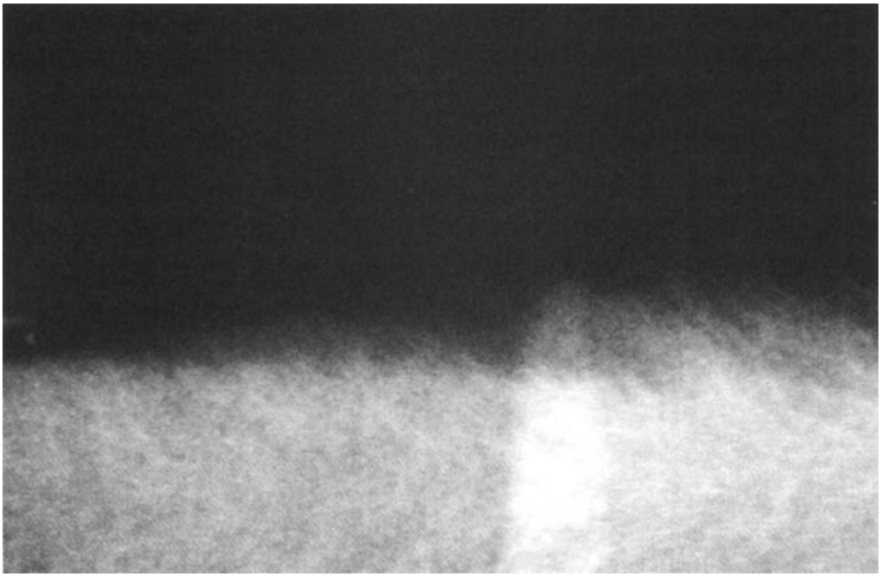

FIGURE 24. Instantaneous flash-pulse particle flow visualization. Flow conditions as in figure 11. Maximum downstream distance displayed is $x = 25.4$ cm.

backward angle with respect to the cross-stream coordinate. Although the perspective of the photograph tends to partially obscure the streak scale, they are seen to become larger as one moves downstream. The intuitive conclusion extracted from this visualization is that these streaks play a major role in the particle dispersion process. Moreover, the lengthscale and spatial correlation that these features seem to have suggests that the large scale of the underlying turbulence must be ultimately responsible for their formation. Hints of the key role played by the large-scale turbulence in the particle dispersion process have been found both numerically (Chung & Troutt 1988; Chien & Chung 1988) and in preliminary experiments (Crowe *et al.* 1988; Kobayashi *et al.* 1988; Lázaro & Lasheras 1989; Longmeir & Eaton 1989). Physically, the idea that the large-scale component of the turbulent motion is responsible for much of the dispersion of the particulate is favoured by the spectral response that the particles have to the different turbulent fluctuations: since the droplets behave essentially as a low-pass filter system, the large eddies, characterized by their large turnover times, are the scales tuned to the particles.

This streak pattern produces a distinct mean concentration profile. It causes asymmetries of the type sketched in figure 25. The instantaneous concentration field created by the passage of one streak with characteristic length $L_s$ superimposed into the core of the spray is given by the broken line. If one accounts for the statistical variation of the streak length $L_s$ and for a decaying concentration law along the streak, the mean profile obtained is similar to the one given by the continuous trace. The associated cross-stream concentration variation is characterized by a strong decay around the average point of the emergence of the streak and a very slow decay for large values of $y$. As a result, the length necessary for the non-dimensional profile to decay to $\frac{1}{2}$ is much smaller than the length needed for the decay from $\frac{1}{2}$ to 0. This profile asymmetry is consistent with the concentration changes found experimentally, especially for large values of the downstream coordinate. In figure 12 it can be seen that for $x = 25.4$ cm, the length necessary for the concentration profile

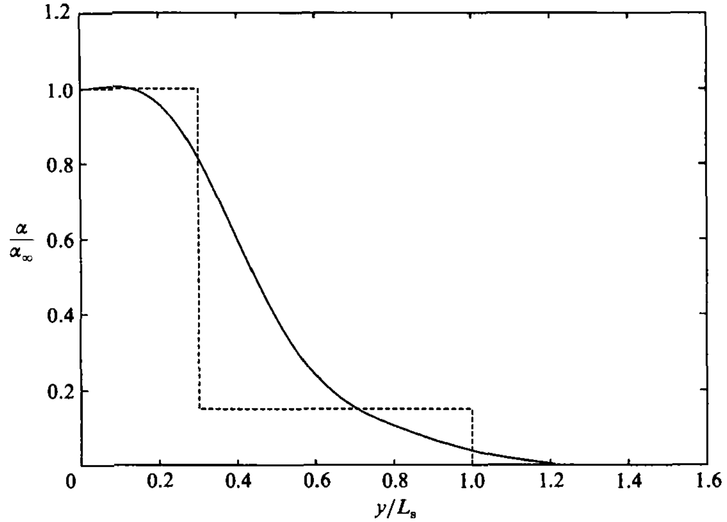

FIGURE 25. Cross-stream particle concentration profile generated by the passage of large-scale streaks. Broken line is the concentration signature of one single, average scale streak. Continuous line represents the statistical outcome due to the passage of a collection of large-scale streaks.

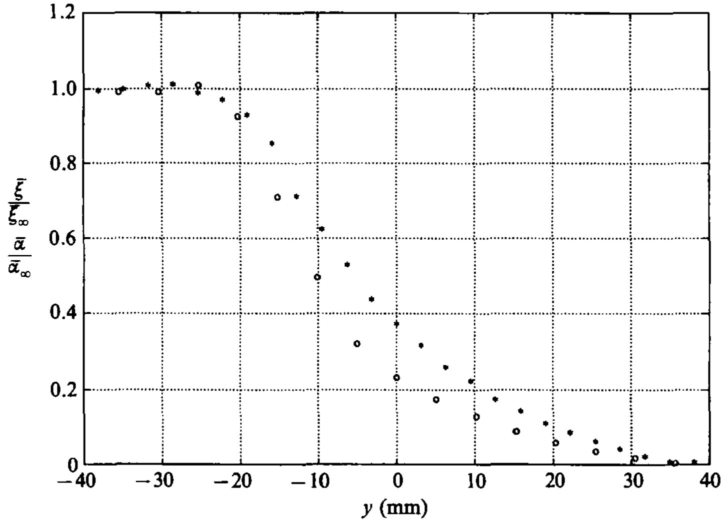

FIGURE 26. Comparison between the non-dimensional mean particle concentration (○) and laser attenuation (*) cross-stream profiles, $x = 25.4$ cm.

to decay to $\frac{1}{2}$ is 15 mm, whereas it takes 45 mm for the decay from $\frac{1}{2}$ to 0 to be completed. This asymmetry contrasts with the behaviour of the gas velocity profile, where both lengths are of the same order of magnitude.

In order to extract more information about the temporal organization of the particle concentration field, $\alpha_p$, the laser attenuation signal, $\xi$, will be used hereafter. Recall that regions richer in small particulate than the unperturbed spray will generate an $\alpha_p/\alpha_{p\infty}$ value smaller than $\xi/\xi_\infty$. This effect can be observed in figure 26, where the values of $\bar{\xi}/\bar{\xi}_\infty$ are higher than those of $\bar{\alpha}_p/\bar{\alpha}_{p\infty}$ in the mixing region. In spite of these differences the qualitative trends are remarkably similar and, as a consequence, allow the attenuation signal to serve as an indicator for studying the temporal structure of the particle concentration field.

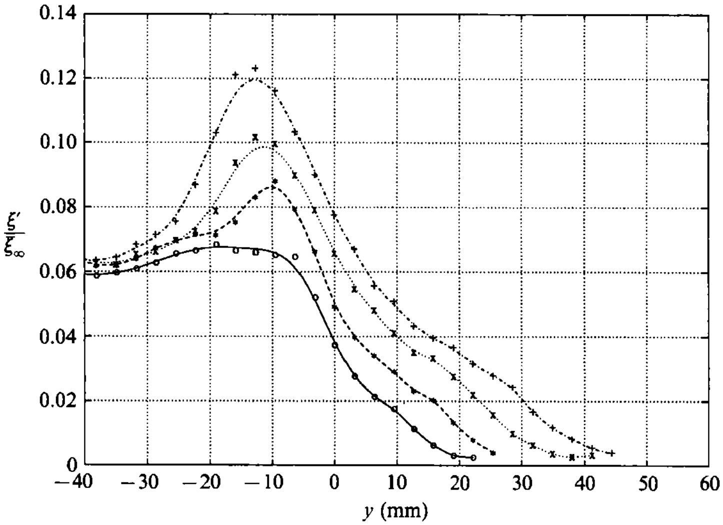

FIGURE 27. Cross-stream profiles of the fluctuating laser attenuation r.m.s.: ○, $x = 10.2$ cm; ∗, 15.2 cm; ×, 20.3 cm; +, 25.4 cm.

The downstream evolution of the non-dimensional r.m.s. of the attenuation intensities, $\xi'/\xi_\infty$, is presented in figure 27. The inhomogeneities of the free-stream spray result in a 6% attenuation fluctuating level, as seen in the leftmost region of the figure. The activity in the fluctuating attenuation is far from reaching equilibrium. The peak in the r.m.s. value is seen to be still growing and has reached, for $x = 25.4$ cm, a value close to 13% of the free-stream attenuation. Also notice that the maximum is located in the negative region of the cross-stream coordinate and its position shifts towards the undisturbed spray as one moves downstream. Another important characteristic observed in these data is the existence of a region, located in the external portion of the dispersion layer, in which the fluctuation level shows a local stabilization in its continuous decay towards the background level. The location of this second region is shown to shift outwards, and its size to increase as one moves farther downstream from the splitter plate.

The above characteristics of the r.m.s. attenuation cross-stream profiles are consistent with the large-streak dispersion picture of figure 25. At every downstream location, since the concentration inside the streaks shows a decay with the distance from the free-stream spray, the attenuation r.m.s. will show its maximum value in the region close to the average point of streak emergence. The fast increase in the r.m.s. attenuation profile from the free-stream to the maximum value is an indication that the presence of this maximum can be associated with the emergence of the streaks, since this is a localized event producing a sharp peak in the r.m.s. profile. In fact, the distance for the peak to form from the free-stream value can be taken as an indication of the variation in the location of the cross-stream coordinate of the emergence point of the streaks. This value is around 10 mm for $x = 25.4$ cm. Furthermore, allowing for a certain backwards curvature in the streaks because of the mean shear, a region of local stabilization in the decay of the fluctuating attenuation will be encountered as we survey cross-stream positions in which the local streak centreline is aligned with the $x$-axis. This effect can be visualized by assuming that a streak passage will create a signature in the attenuation given by a pulse with width, depending upon the width of the streak. The r.m.s. value associated with a set of pulses with a width-to-period ratio (the *duty cycle*) $w$ is

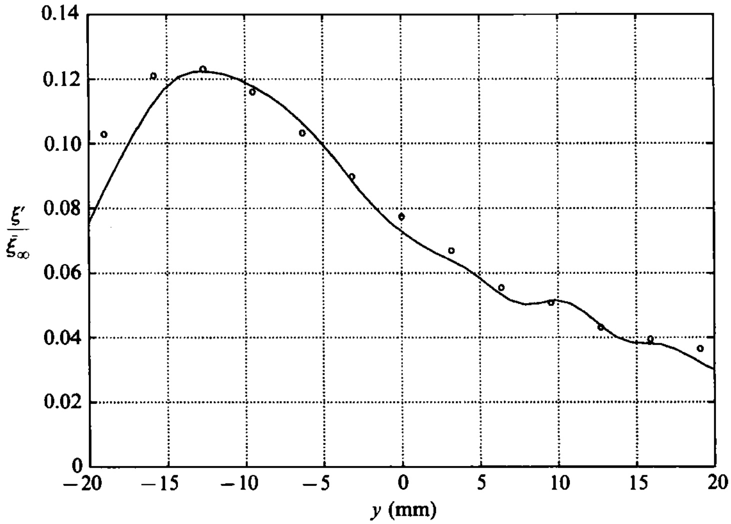

FIGURE 28. Cross-stream fluctuating attenuation r.m.s. profile (○) compared with a computed cross-stream derivative of the mean attenuation $-k\,\mathrm{d}\bar{\xi}/\mathrm{d}y$ (——), $x = 25.4$ cm.

proportional to $w-w^2$. Therefore, it is maximum when $w = \frac{1}{2}$. For thin streaks the duty cycle at the root of the streak is low (of the order of 0.1). Consequently, as the streaks are bent by the shear, the duty cycle increases, resulting in an increase in the attenuation r.m.s.

The relation between the mean and r.m.s. attenuation profiles is shown in figure 28, where the r.m.s. of the attenuation is compared, in the layer, to a computed derivative of the mean attenuation. The mean profile is approximated using a least-squares fit by cubic splines. The derivative is then computed as the forward difference from the approximating data. Finally, a scale factor is applied to bring the calculated level to the level shown by the r.m.s. profile. Therefore, the continuous line is an approximation to the r.m.s. fluctuation given by

$$\xi'_c = -k\,\mathrm{d}\bar{\xi}/\mathrm{d}y, \tag{65}$$

with $k = 3.75$ mm. Considering the inherent risk in the computation of a derivative from discrete data prone to introducing high-wavenumber noise, the curve seems to reproduce the experimental data reasonably well. However, as one approaches the free stream, the correlation between measurements and fitting curve is lost.

The spectral analysis of the fluctuating attenuation signal reveals further details about the particle dispersion field. Figure 29 presents the evolution, at several downstream locations, of the attenuation spectra measured at $y = 0$. A band of enhanced spectral content can be identified at each curve. Furthermore, this band is found to shift towards the low-frequency regions of the spectrum as one moves downstream. These two characteristics lead to the identification of this portion of the spectra with the dispersion created by the large-scale vortices. The impact that this band has on the fluctuating attenuation is important. The r.m.s. attenuation percentage contained in the frequencies having a spectral level above the baseline observed at very low frequencies varies from 84% at $x = 7.6$ cm to 89% at $x = 25.4$ cm. Most of the attenuation activity can, therefore, be attributed to the coherent band.

A frequency characterizing the band is that for which the spectrum shows a maximum value. Adjusting a parabola to the spectral data in the coherent region and

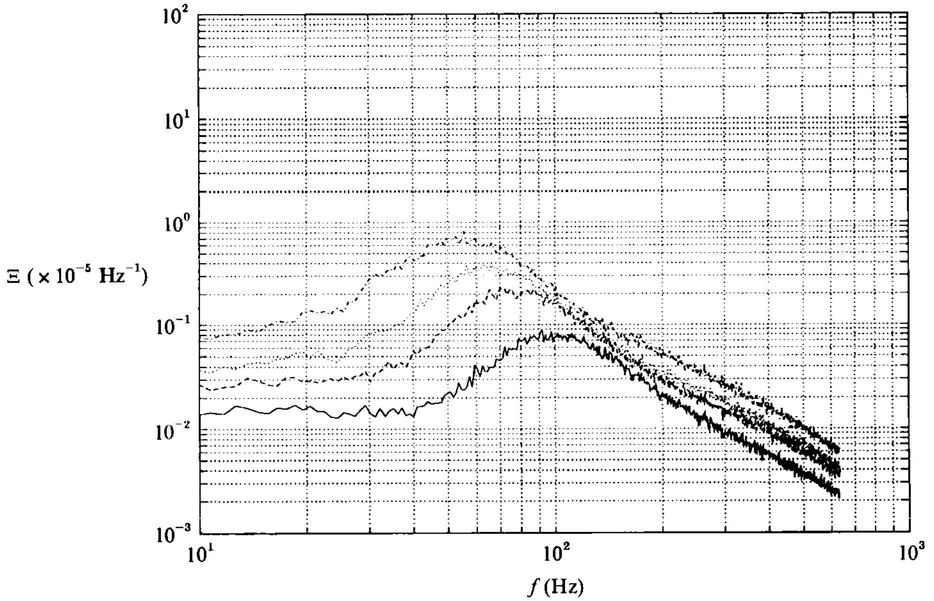

FIGURE 29. Downstream evolution of the laser attenuation temporal power spectrum, $y = 0$. ——, $x = 7.6$ cm; ----, 12.7 cm; ......., 17.8 cm; —·—·—, 25.4 cm.

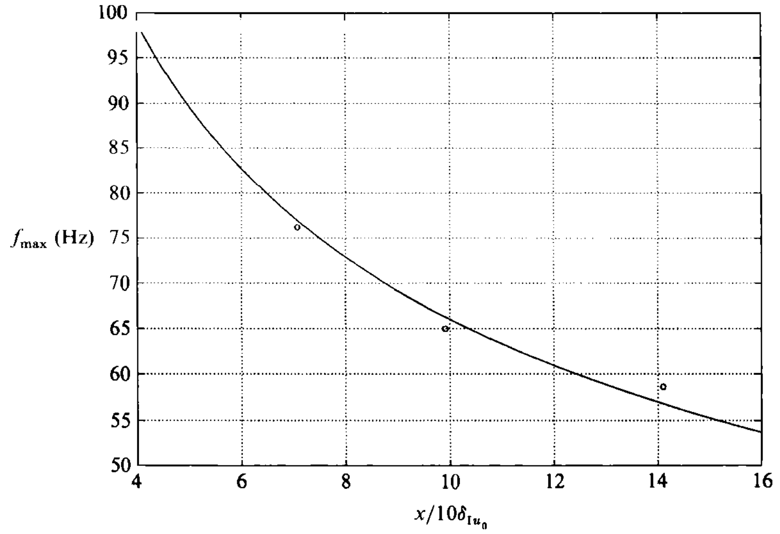

FIGURE 30. Downstream variation of the frequency of maximum laser attenuation power spectrum, $y = 0$: ○, experimental data; —, equation (66).

computing its maximum gives the evolution of the preferred frequency shown in figure 30.

Assuming a power-law variation of the preferred frequency with the downstream distance, a least-squares fit gives

$$f_{\max} = 501(x/\delta_{Iu_0})^{-0.44} \tag{66}$$

($f$ in Hz). The high-frequency portion of the spectra can also be approximated by a power law. In the range $400 < f < 900$ Hz, the exponent is seen to vary from $-1.96$

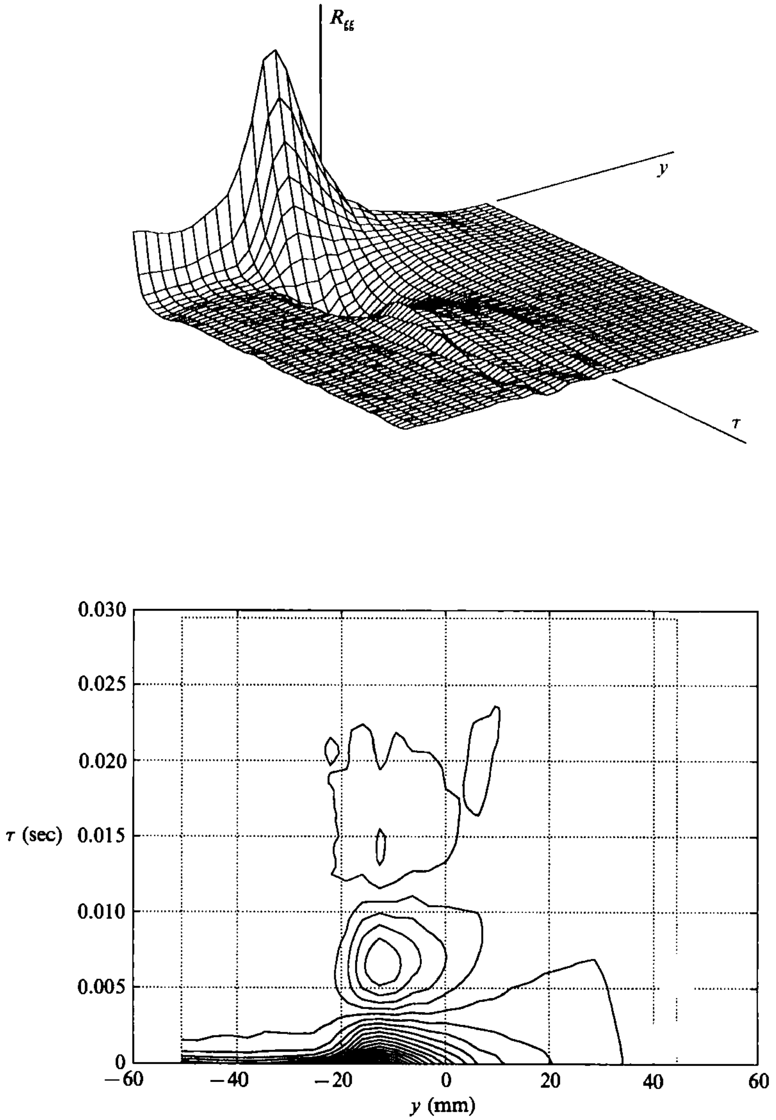

FIGURE 31. Cross-stream variation of the laser attenuation temporal autocorrelation function $x = 25.4$ cm: (*a*) autocorrelation surface, (*b*) isocontour plot.

at $x = 7.6$ cm to $-2.07$ at $x = 25.4$ cm. The corresponding values for the longitudinal air velocity fluctuations were $-1.40$ and $-1.55$ respectively. Therefore, the high-frequency decay is faster for the particle concentration field than for the gas velocity fluctuations, a result expected because of the low-pass filter nature of the particles.

The organization of the temporal attenuation autocorrelation, $R_{\xi\xi}(\tau) = \overline{\xi(t)\,\xi(t+\tau)}$, along the cross-stream coordinate is shown in figure 31 together with its contour plot. The presence of the large coherent scale is seen to cover most of the dispersion region. In addition, note the slight asymmetry of the contour plot towards the outer edge of the mixing layer. This asymmetry is also responsible for the local plateau in the r.m.s. decay observed in the external dispersion layer and can be associated with the alignment of the streaks centreline with the $x$-axis in the outer portion of the mixing layer.

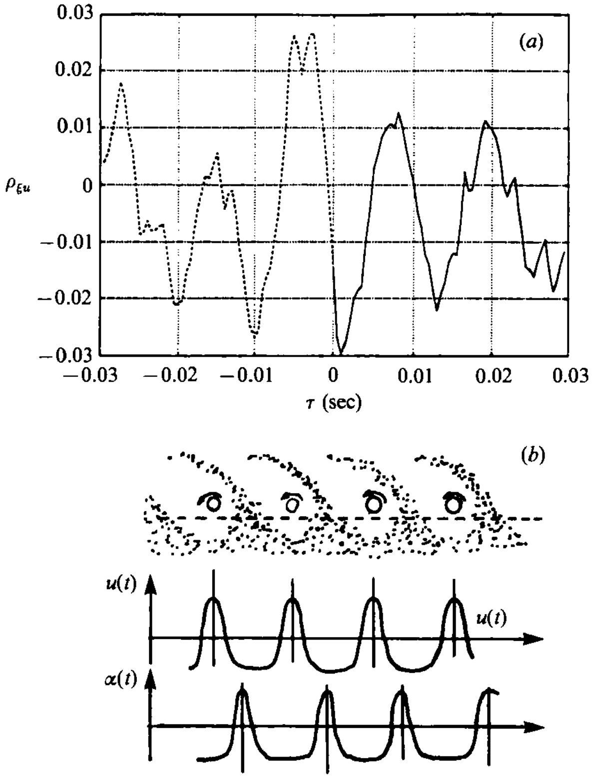

FIGURE 32. (a) Laser attenuation-gas velocity temporal cross-correlation coefficient, $x = 203$ mm, $y = -9.5$ mm. (b) Reconstruction of the gas velocity and particle concentration field.

The spectral measurements revealed a much higher degree of organization and coherency in the fluctuating attenuation signal than the one found in the longitudinal gas velocity. This seems to be consistent with the enhanced response expected from the particles to low-frequency fluctuations. It must be pointed out, however, that the two measurements are very different in nature: whereas the hot wire measures the velocity field at a given point, the attenuation signal gives a $z$-average measurement of the particle concentration. Nevertheless, the appearance of a coherent band in the attenuation spectra indicates an important degree of two-dimensionality in the coherent fluctuations or, otherwise, the integration along $z$ would prevent the coherent band from appearing so clearly.

With the available experimental data, a quantity that can give further insight into the relation between the turbulent velocity field and the particle dispersion response is the term $\overline{\xi u}$, which is related to the particle turbulent transport $\overline{\alpha_p u_p}$. In this study, we conducted measurements of $\overline{\xi u}$ up to $x = 20.3$ cm. The data reveals very small $\overline{\xi u}$-values. Only for the farthest downstream positions measured, were negative values of $\overline{\xi u}$ above the noise level found in the region close to $y = -10$ mm (the point where the attenuation r.m.s. shows its maximum). The temporal cross-correlation coefficient

$$\rho_{\xi u}(\tau) = \frac{\overline{\xi(t)\,u(t+\tau)}}{\overline{\xi^2(t)}^{\frac{1}{2}}\,\overline{u^2(t)}^{\frac{1}{2}}} \tag{67}$$

is shown in figure 32. For negative values of $\tau$ the relation $\rho_{\xi u}(-\tau) = \rho_{u\xi}(\tau)$ was used. A clear repetitive pattern is seen to characterize this cross-correlation. A tentative reconstruction of the fluctuating velocity and attenuation fields is sketched in figure 32(*b*) as well. The positive areas of the cross-correlation are displaced with respect to the $\tau = 0$ point, indicating that the streak emergence region is displaced with respect to the vortices' core. Also, an area of reduced particle concentration is located around the vortices' cores, providing a region of negative cross-correlation close to $\tau = 0$.

The period characterizing this repetitive particle depletion and lifting is given by the difference between the value of $\tau$ corresponding to two consecutive maxima or minima. An estimated value from the data in figure 32 gives $T \approx 0.013$ s, corresponding to a frequency $f = 77$ Hz.

## 10. Conclusions

The dispersion properties of small water particles in a naturally developing, high-Reynolds-number, turbulent plane mixing layer have been investigated.

Flow visualizations as well as spectral analysis of the particle attenuation revealed the central role played by the large-scale turbulent motion in the particle dispersion process. The instantaneous structure of the dispersion layer was found to be characterized by the existence of large-scale streaks emanating from the undisturbed spray. Cross-correlation measurements between the particle obscuration and the gas velocity showed that the average location of the streak emergence point occurred in the braid regions separating two consecutive large-scale vortices of the mixing layer.

The mean dispersion field resulted from a statistical distribution of these large-scale coherent streaks. For all the particle sizes, the particle concentration thicknesses exhibited smaller values than the momentum thickness of the turbulent base flow. In addition, all the particle concentration thicknesses were shown to be characterized by an initial induction region with no appreciable growth, followed by an asymptotic state, whose growth rate approached that of the momentum thickness of the base flow. Furthermore, it was found that the extension of the induction region scaled with the particle size and that when both downstream and cross-stream coordinates were non-dimensionalized with a distance proportional to the square of the particle diameter, a universal, mean-particle-diameter-independent dispersion field was obtained. The selected non-dimensionalization was shown to be consistent with the time-averaged equations of small, heavy particles dispersing in a mean velocity self-similar turbulent flow.

Resulting from the particle size scaling of the induction region, the dispersion layer was shown to be characterized by a strong selective dispersion action whereby the central core of the mixing region exhibited an enhanced presence of small particulate. In addition, this central dispersion area was found to be flanked by two external sublayers where local accumulation of larger particulate occurred.

This work was supported by the US–Spain Joint Committee for Scientific and Technological Cooperation (Project CCA-8510-057), by an equipment Grant from NSF (No. MEA-8405811), and by a grant from ONR (No. N00014-91-J-1252). Partial support from United Technologies Corporation is also acknowledged. The material presented here is in great part extracted from the Ph.D. Dissertation of B. J. Lázaro conducted at the University of Southern California.

## REFERENCES

Bachalo, W. D. & Houser, M. J. 1984 Phase doppler spray analyzer for simultaneous measurements of drop size and velocity distribution. *Opt. Engng* **23**, 583–590.

BEARMAN, P. W. 1971 Corrections for the effect of ambient temperature drift on hot-wire measurements in incompressible flows. *DISA Info.* **11**, 25–30.

BROWAND, F. K. & LATIGO, B. O. 1979 Growth of the two-dimensional mixing layer from a turbulent and nonturbulent boundary layer. *Phys. Fluids* **22**, 1011–1019.

BROWN, G. L. & ROSHKO, A. 1974 On density effects and large structure on turbulent mixing layers. *J. Fluid Mech.* **64**, 775–816.

CALL, C. J. & KENNEDY, I. M. 1990 Droplet dispersion in a round turbulent jet. *AIAA 28th Aerospace Sci. Meeting, Paper* 90-468.

CHEIN, R. & CHUNG, J. N. 1988 Simulation of particle dispersion in a two-dimensional mixing layer. *AIChE J.* **34**, 946–954.

CHUNG, J. N. & TROUTT, T. R. 1988 Simulation of particle dispersion in an axilsymmetric jet. *J. Fluid Mech.* **186**, 199–222.

CROWE, C. T., CHUNG, J. N. & TROUTT, T. R. 1988 Particle mixing in free shear flows. *Prog. Energy Combust. Sci.* **14**, 171–194.

DREW, D. A. 1983 Mathematical modelling of two-phase flows. *Ann. Rev. Fluid Mech.* **15**, 261–291.

HINZE, J. O. 1975 *Turbulence.* 2nd Edn. McGraw-Hill.

HJELMFELT, A. T. & MOCKROS, L. J. 1966 Motion of discrete particles in a turbulent fluid. *Appl. Sci. Res.* **16**, 149–161.

HOTTEL, H. C., SAROFIM, A. F., VASALOS, I. A. & DALZELL, W. H. 1970 Multiple scatter: comparison of theory with experiment. *J. Heat Transfer* **92**, 285–291.

HUNT, J. C. R. 1985 Turbulent diffusion from sources in complex flows. *Ann. Rev. Fluid Mech.* **7**, 447–485.

KOBAYASHI, H., MASUTANI, S. M., AZUATA, S., ARASHI, N. & HISHINUMA, Y. 1988 Dispersed phase transport in a plane mixing layer. In *Transport phenomena in turbulent flows*, pp. 433–446. Hemisphere.

LÁZARO, B. J. 1989 Particle dispersion in turbulent free shear flows. Ph.D. Dissertation, University of Southern California.

LÁZARO, B. J. & LASHERAS, J. C. 1989 Particle dispersion in a turbulent, plane, free shear layer. *Phys. Fluids* A **1**, 1035–1044.

LÁZARO, B. J. & LASHERAS, J. C. 1992 Particle dispersion in the developing free shear layer. Part 2. Forced flow. *J. Fluid Mech.* **235**, 179–221.

LONGMIER, E. K. & EATON, J. K. 1989 Structure and control of particle laden round jets. *Proc. Korean–US Fluid Engng Seminar*, pp. 435–454.

MAXEY, M. R. & RILEY, J. J. 1983 Equation of motion for a small sphere in a nonuniform flow. *Phys. Fluids* **26**, 883–889.

PERRY, A. E. 1982 *Hot Wire Anemometry.* Clarendon.

SNYDER, W. H. & LUMLEY, J. L. 1971 Some measurements of particle velocity autocorrelation functions in a turbulent flow. *J. Fluid Mech.* **48**, 41–71.

SWITHENBANK, J., BEER, J. M., TAYLOR, D. S., ABBOT, D. & MCCREATH, G. C. 1976 A linear diagnostic technique for the measurement of droplet and particle size distribution. *AIAA 14th Aerospace Sci. Meeting*, pp. 421–447.

TAYLOR, G. I. 1921 Diffusion by continuous movements. *Proc. R. Soc.Lond.* **151**, 421–478.

THOMPSON, D. J. 1987 Criteria for the selection of stochastic models of particle trajectories in turbulent flows. *J. Fluid Mech.* **180**, 509–526.

VAN DE HULST, H. C. 1957 *Light Scattering by Small Particles.* Dover.

WEISBROT, I., EINAV, S. & WYGNANSKI, I. 1982 The nonunique rate of spread of the two-dimensional mixing layer. *Phys. Fluids* **25**, 1691–1693.